



RESEARCH ARTICLE

10.1029/2022JG007330

Key Points:

- Our study site in the Indigirka Lowlands shows strong (-0.0039 NDVI units yr^{-1}) and ubiquitous (76% of area) recent browning in Landsat NDVI
- High snowfall and low summer rainfall were associated with lower summer NDVI, with differential impacts across topographical gradients
- Local small-scale shifts in vegetation types and thermokarst activity show weak association with Landsat NDVI trends

Supporting Information:

Supporting Information may be found in the online version of this article.

Correspondence to:

R. Í. Magnússon,
runa.magnusson@wur.nl

Citation:

Magnússon, R. Í., Groten, F., Bartholomeus, H., van Huissteden, K., & Heijmans, M. M. P. D. (2023). Tundra browning in the Indigirka Lowlands (North-eastern Siberia) explained by drought, floods and small-scale vegetation shifts. *Journal of Geophysical Research: Biogeosciences*, 128, e2022JG007330. <https://doi.org/10.1029/2022JG007330>

Received 5 DEC 2022

Accepted 11 JUL 2023

Author Contributions:

Conceptualization: Rúna Í. Magnússon, Finn Groten

Formal analysis: Rúna Í. Magnússon, Finn Groten

Funding acquisition: Monique M. P. D. Heijmans

Investigation: Rúna Í. Magnússon, Finn Groten

Methodology: Rúna Í. Magnússon, Finn Groten, Harm Bartholomeus

Project Administration: Rúna Í. Magnússon, Monique M. P. D. Heijmans

Tundra Browning in the Indigirka Lowlands (North-Eastern Siberia) Explained by Drought, Floods and Small-Scale Vegetation Shifts

Rúna Í. Magnússon¹ , Finn Groten¹ , Harm Bartholomeus², Ko van Huissteden³, and Monique M. P. D. Heijmans¹

¹Plant Ecology & Nature Conservation Group, Wageningen University, Wageningen, the Netherlands, ²Laboratory for Geo-information Science & Remote Sensing, Wageningen University, Wageningen, the Netherlands, ³Faculty of Science, Vrije Universiteit, Amsterdam, the Netherlands

Abstract Contrary to the general “greening of the Arctic”, the Siberian Indigirka Lowlands show strong “browning” (a decrease in the Normalized Difference Vegetation Index or “NDVI”) in various recent satellite records. Since greening and browning are generally indicative of increases and losses in photosynthetically active biomass, this browning trend may have implications for the carbon balance and vegetation of this Arctic tundra region. To explore potential mechanisms responsible for this trend break from general Arctic greening, we studied timeseries of Landsat summer maximum NDVI, weather data, and high-resolution maps of vegetation compositional change, topography, geomorphology and hydrology. We find that a significant proportion of browning (lower summer NDVI) is explained by moisture dynamics, with high snow depths and resulting floods as well as summer drought coinciding with low NDVI. Relations between seasonal weather variables and NDVI are spatially heterogeneous, with floodplains, drained thaw lake basins and Yedoma ridges showing different patterns of association with weather variables. Low summer NDVI after high snowfall was particularly evident in floodplains, likely explained by early summer floods. Local small-scale vegetation changes explained only small amounts of variance in browning rates in Landsat NDVI. Local expansion of *Sphagnum* vegetation in particular may have contributed to recent browning of our study site, but higher resolution NDVI timeseries are necessary to accurately constrain the role of small-scale vegetation shifts. Overall, associations identified in this study suggest that future increases in Arctic precipitation variability and extremes may limit tundra greening, but to different extents even across comparatively small topographical contrasts.

Plain Language Summary Across Arctic regions, satellite images show that tundra ecosystems have been “greening”. This suggests that plant growth, and thereby uptake of carbon from the atmosphere, is increasing in the Arctic. The Indigirka Lowlands in Siberia provide a stark contrast; in this lowland tundra region, satellite images show “browning”, which suggests a decline in plant growth. We explored why this might be the case, in order to better assess whether browning should be expected across the wider Arctic in a changing climate. We compare local browning rates, calculated as changes in spectral indices from Landsat satellite images, to annual weather data, detailed maps of local vegetation changes and maps of terrain properties such as elevation and hydrology. We find that browning is associated with high snow depths and resulting floods, but also with dry summer conditions. Browning was not strongly related to local, small-scale changes in vegetation (the most common of which was expansion of peat moss). We also find that the degree of association with potential drivers of browning (e.g., flooding, dry summers) differs across landforms. Floodplains show particularly strong browning following high snowfall, likely explained by early summer floods. This suggests that expected increases in year-to-year variability and extremes in Arctic precipitation may limit future greening.

1. Introduction

One of the main manifestations of rapid climate warming in the Arctic is an increase in “greenness” of the terrestrial Arctic (Berner et al., 2020; Box et al., 2019; Frost, Macander, et al., 2021; Mekonnen et al., 2021; Myers-Smith et al., 2020). Arctic greening is evident from a large number of studies and generally refers to increases in vegetation biomass or other productivity measures (Myers-Smith et al., 2020). Such observations may be derived

© 2023. The Authors.

This is an open access article under the terms of the [Creative Commons Attribution License](https://creativecommons.org/licenses/by/4.0/), which permits use, distribution and reproduction in any medium, provided the original work is properly cited.

Resources: Rúna Í. Magnússon, Ko van Huissteden, Monique M. P. D. Heijmans
Supervision: Rúna Í. Magnússon, Harm Bartholomeus, Ko van Huissteden, Monique M. P. D. Heijmans
Visualization: Rúna Í. Magnússon, Finn Groten
Writing – original draft: Rúna Í. Magnússon, Finn Groten
Writing – review & editing: Rúna Í. Magnússon, Finn Groten, Harm Bartholomeus, Ko van Huissteden, Monique M. P. D. Heijmans

from various types of studies (e.g., vegetation monitoring, warming experiments, remote sensing studies) and the term “greening” has different meanings and implications in these various fields (Myers-Smith et al., 2020). In remote sensing literature, including this study, greening and browning refer to an increase and decrease in NDVI (Normalized Difference Vegetation Index) or other vegetation index. NDVI is the most commonly used vegetation index and generally considered most suitable for monitoring of Arctic vegetation trends (Myers-Smith et al., 2020). Increases in vegetation productivity on a pan-Arctic scale are expected to result in enhanced uptake of CO₂ (McGuire et al., 2018; Meredith et al., 2019), but it is currently unclear how large this uptake may be and how large a proportion of increasing Arctic carbon emissions (for instance from thawing permafrost) it may compensate (Abbott et al., 2016; McGuire et al., 2018; Meredith et al., 2019; Turetsky et al., 2020; Zona et al., 2022). In addition, despite its capability to remotely quantify general patterns of photosynthetically active vegetation, it is often unclear how NDVI changes relate to real-world changes in vegetation properties and composition and to changes in ground surface properties other than vegetation (Beamish et al., 2020; Myers-Smith et al., 2020). This complicates interpretation and forecasting of NDVI trends for the Arctic.

The Siberian Indigirka Lowlands (Figure 1b) are currently showing a trend break toward pronounced and increasing browning in various long term coarse to moderate resolution satellite records (Figure 1a) (Berner et al., 2020; Frost, Macander, et al., 2021; Magnússon et al., 2021; Mekonnen et al., 2021). Positive NDVI trends have been observed in this region prior to 2008 (Bhatt et al., 2010). Although most tundra regions continue to show increases in NDVI (Frost, Macander, et al., 2021), recent evidence suggests that regional browning is increasing across the wider Arctic. Based on Landsat records, the estimated percentage area of the Arctic tundra biome that shows significant browning has increased from 4.5% (1985–2016) to 6.0% (2000–2016) and recently 8% (2000–2020) (Berner et al., 2020; Mekonnen et al., 2021). Browning generally manifests on smaller spatial scales and shorter timeframes compared to the overall trend of Arctic greening (Myers-Smith et al., 2020). Improved understanding of the drivers behind increasing regional browning is necessary to identify potential limits to future Arctic greening (Frost, Macander, et al., 2021) and associated carbon uptake in a rapidly changing and heterogeneous Arctic biome.

Browning can indicate a decrease in vegetation foliage (Myers-Smith et al., 2020; Phoenix & Bjerke, 2016), which may have detrimental consequences for the photosynthetic capacity and carbon sink strength of tundra regions (Treharne et al., 2019). NDVI trends are often linked with change in shrub abundance in particular (Blok, Schaeppman-Strub, et al., 2011; Boelman et al., 2011; Forbes et al., 2010; Martin et al., 2017) while the role of other vegetation communities in determining NDVI is less recognized in literature (Heijmans et al., 2022). Changes in vegetation foliage may in turn be caused by extreme weather events, outbreaks of defoliating insects, permafrost thaw, flooding and other mechanisms (Frost, Macander, et al., 2021; Myers-Smith et al., 2020; Phoenix & Bjerke, 2016). Apart from changes in vegetation, presence of snow or hydrological changes such as flooding or drainage may directly decrease NDVI values due to changes in infrared reflectance (Goswami et al., 2011; Reynolds & Walker, 2016). Increases in surface water presence are associated with browning on a panarctic scale (Li et al., 2021). Lastly, NDVI dynamics strongly depend on the spatial scale over which they are quantified (Beamish et al., 2020; Myers-Smith et al., 2020). Coarser-resolution data are limited in their ability to detect smaller-scale patterns that may yield information on the extent and underlying mechanisms of browning (Bhatt et al., 2013), while high resolution data generally has limited temporal availability (Beamish et al., 2020; Myers-Smith et al., 2020). Strategically linking spatially limited high-resolution data to coarser regional and panarctic NDVI records is a key research priority in Arctic greening studies (Myers-Smith et al., 2020) and may explain why particular regions like the Indigirka Lowlands are browning.

NDVI dynamics in the Indigirka Lowlands may be related to various recent trends or disturbances on the ground and may thereby contain valuable information on the development of vegetation and permafrost in this remote and understudied Arctic ecosystem. In ice-rich permafrost landscapes such as the Indigirka Lowlands (Nitzbon et al., 2020), thermokarst activity can cause local waterlogging and rapid vegetation shifts from shrub dominated vegetation towards aquatic plant communities (Li et al., 2017; Magnússon et al., 2021). Such vegetation disturbance and recovery dynamics can manifest as distinct local browning events and subsequent greening (Reynolds & Walker, 2016; Verdonen et al., 2020; Zona et al., 2010). It is unclear however to what extent such highly localized (sub-meter to meter scale) processes are reflected in coarser-scale regional NDVI dynamics. In addition, the Indigirka Lowlands have experienced several recent weather extremes, including record high snowfall in 2016–2018 causing widespread flooding (Tei et al., 2020) and extremely warm and dry spring and summer conditions in 2019–2020 (Overland & Wang, 2021). We aim to assess to what extent these various processes

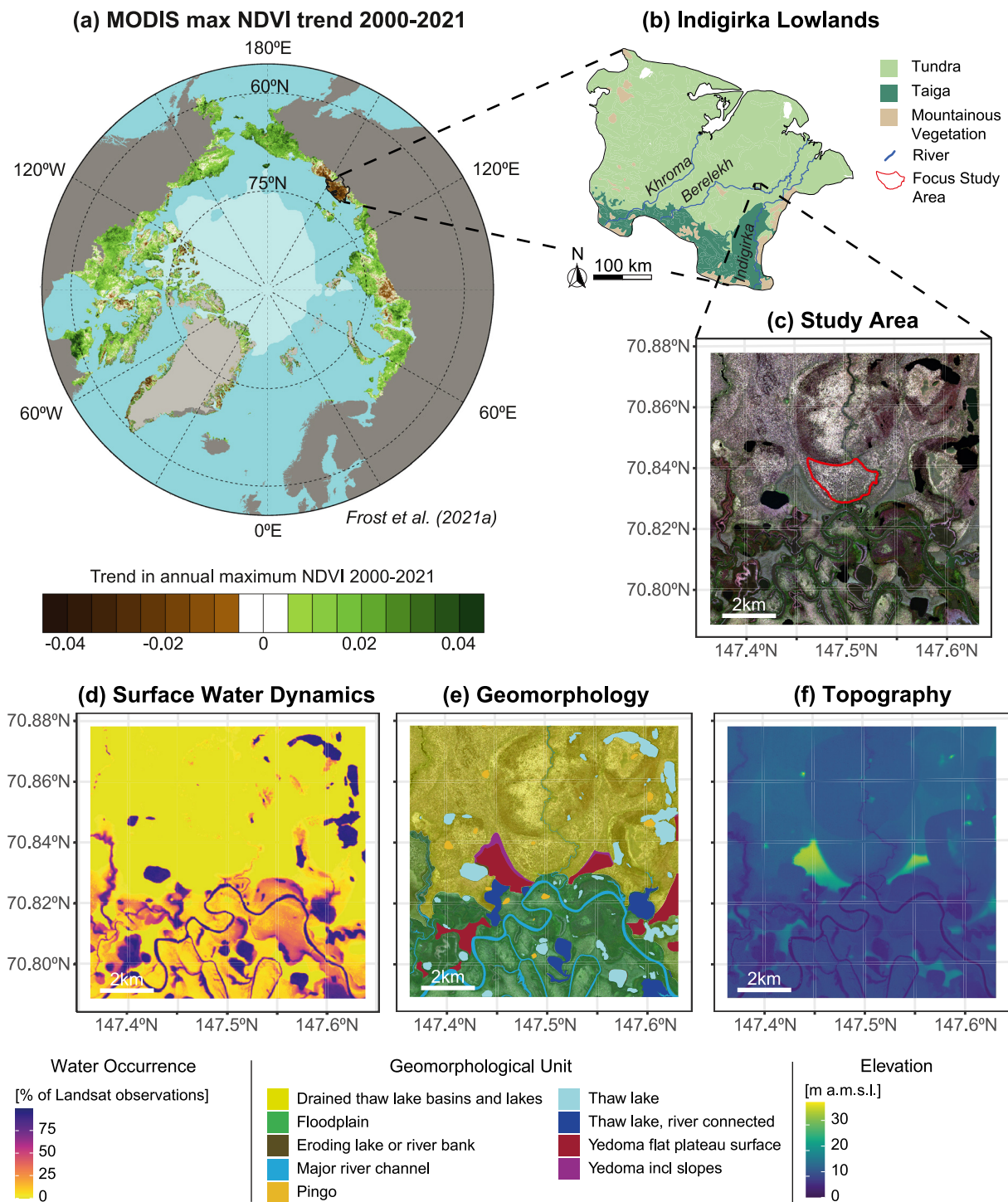


Figure 1. Study Site and its context within recent Arctic greening/browning dynamics. (a) Adapted from Frost, Macander, et al. (2021). MODIS NDVI trends for the entire Arctic (2000–2021) from Frost, Macander, et al. (2021)'s report on Tundra Greenness. The Indigirka Lowlands are indicated with a black outline. (b) The Indigirka Lowlands and its main vegetation zones and water bodies. White areas represent large lakes. (c) 2019 WorldView-2 satellite image of the study area. WorldView © MAXAR, 2019. The red outline indicates the extent of the vegetation maps generated by Magnússon et al. (2021) that were used for this study. (d) Surface water occurrence, expressed as the percentage of available Landsat observations in which the pixel was classified as surface water. Retrieved from the Global Surface Water Map (Pekel et al., 2016). (e) Main geomorphological units in the study area, from Van Huissteden and Belelli Marchesini (2014). Main units (floodplains and drained thaw lake basins and lakes) are shown as a transparent overlay over the satellite image of Figure 1c, while subunits are shown as opaque features. (f) Topography of the study area from the Arctic DEM (Porter et al., 2018).

are associated with recent browning in the Indigirka Lowlands, and whether the role of these processes differs throughout the landscape.

To identify potential patterns and causes of browning in this rapidly changing North-Eastern Siberian tundra ecosystem, we investigate associations between various NDVI products (based on 2 m resolution commercial WorldView-2 and GeoEye-1 images, 30 m resolution Landsat images and 10 m resolution Sentinel images), vegetation cover dynamics, thematic map data, surface water dynamics and weather data. We expected recent browning to be related to thermokarst-induced formation of small waterbodies and subsequent shifts to aquatic vegetation communities (Magnússon et al., 2021), spring and early summer flood events (Tei et al., 2020) and recent heatwaves and drought (Overland & Wang, 2021). However, we expected that different types of processes that contribute to browning likely manifest on different spatial and temporal scales (Myers-Smith et al., 2020). By elucidating drivers of Arctic tundra greening and browning dynamics using a multi-scale approach and a wide range of spatially detailed information we contribute to assessment of Arctic greening/browning dynamics in a rapidly changing climate.

2. Materials and Methods

2.1. Study Area

NDVI trends and their relation to vegetation changes, weather trends, hydrology and terrain were studied in a 10 by 10 km area in the “Kytalyk” Nature Reserve in north-eastern Siberia (70°49'N, 147°29'E) (Figure 1c). This lowland area consists of floodplains and drained thaw lake basins or “alases”, interspersed with remnants of older Yedoma deposits (Figure 1e). Local soils consist of a shallow 30–46 cm active layer overlaying continuous permafrost. Soils have organic layers of typically 10–25 cm, overlying mineral soil with silt to clay texture (Siewert et al., 2015). The upper permafrost layer contains 75% ice by volume on an average, making the region prone to thermokarst (Iwahana et al., 2014). Mean annual temperature and precipitation were -12.7°C and 189 mm and average July temperature and precipitation were 10.6°C and 22 mm for the period 1990–2020 (RIHMI-WDC, 2020) (Figure S1 in Supporting Information S1). The growing season (with mean daily temperature above zero degrees and snow free conditions) is short and generally lasts from June to August (Van der Molen et al., 2007).

Local vegetation is classified as a mixture of tussock sedge (*Eriophorum vaginatum*), dwarf shrub and moss tundra (type G4) and erect dwarf-shrub tundra (type S1) by the circumpolar Arctic vegetation map (Raynolds et al., 2019), which is typical vegetation for this region (Troeva et al., 2010). In earlier studies at this field site, six vegetation classes (shrub, tussock, lichen, sedge, *Sphagnum* and open water) have been distinguished based on the dominant plant functional type (Magnússon et al., 2021; Siewert et al., 2015). Tussock sedge is found in elevated landscape positions such as Yedoma remnants and pingos. Shrub and lichen are found on slightly elevated ice wedge polygon rims and slightly elevated (± 0.5 m) areas with high ground ice content (Wang et al., 2019). Aquatic sedges and *Sphagnum* are present in lower elevation sites such as low center polygons, diffuse drainage systems and thaw ponds. Floodplains are generally dominated by sedges, willow shrubs, peat moss and grasses (Magnússon et al., 2021; Siewert et al., 2015). Apart from lakes and streams, small open water features are found in polygonal tundra, in isolated thaw ponds and in diffuse drainage systems (Magnússon et al., 2021). Detailed vegetation maps are available from Magnússon et al. (2021) for a sub-area representing a single alas (Figure 1c), which was used as a focus area to study relations between vegetation compositional changes and NDVI trends.

2.2. Data Acquisition

2.2.1. Very High Spatial Resolution NDVI Images

NDVI images (2 m) were generated from three commercial very high resolution satellite images (Table S1 in Supporting Information S1). A GeoEye-1 image was available for 19 August 2010, and WorldView-2 images were available for 10 July 2015 and 1 August 2019. The geometrically rectified images were atmospherically corrected by MAXAR Inc. (Denver, Colorado, USA) using AComp processing (MAXAR n.d.) to reduce possible NDVI bias due to changing illumination, viewing geometries and atmospheric conditions (Pacifi et al., 2014). After atmospheric correction, NDVI was calculated for all three images (2010, 2015, and 2019) from red (RED) and near-infrared (NIR) surface reflectance according to Equation 1 (Tucker, 1979).

$$NDVI = \frac{NIR - RED}{NIR + RED} \quad (1)$$

2.2.2. Functional Vegetation Maps

Three very high resolution (0.5 m) maps of functional vegetation groups (FVGs) were available (Magnússon et al., 2021), produced for a subsite within the study area (Figure 1c). These maps classified the same very high resolution satellite images from 2010, 2015 and 2019 (Section 2.2.1, Table S1 in Supporting Information S1) into areas dominated by shrub, tussock, lichen, sedge or *Sphagnum*, or open water features (six FVGs in total). Individual images achieved high overall classification accuracy (91%–93%) when compared to field vegetation observations. Compared to field-observed shifts in dominant vegetation communities, classified vegetation changes between 2010 and 2019 had an overall accuracy of 75%. These FVG maps were produced from pan-sharpened images using a random forest classification with spatio-temporal Potts model regularization. The Potts model algorithm ensures consistent classification among images by penalizing differences in class labels among spatially and temporally adjacent pixels, so that changes in class labels over time and among neighboring pixels are only allowed if spectral differences among pixels are sufficiently large (Magnússon et al., 2021; Potts, 1952). With high overall accuracies and a consistent classification scheme among images, these maps provide a good basis for comparison of NDVI products to vegetation composition. Apart from classified FVG maps, pixel class probabilities were derived from the initial Random Forest classification (prior to Potts model regularization).

2.2.3. Landsat Annual maxNDVI Time Series

An NDVI time series (1999–2019) was generated for the study site from LEDAPS corrected Landsat 7 & 8 surface reflectance imagery obtained from Google Earth Engine (Gorelick et al., 2017). Like most of the Arctic, this site lacks Landsat data from prior to 1999. NDVI values were calculated for each image using Equation 1 (Tucker, 1979). For each year the maximum NDVI per pixel was computed from all images between July 20th and August 5th, which corresponds with the peak of the local growing season (Blok, Sass-Klaassen, et al., 2011; Van der Molen et al., 2007). After visual inspection, images that appeared to be cloud covered by more than 50% (including clouds not detected by CFmask) were filtered out. To account for sensor discrepancies between Landsat 7 and 8, Landsat eight images were transformed using locally parametrized linear regression (Roy et al., 2016). Such locally parameterized corrections are commonly used in order to compare NDVI values between Landsat 8 and Landsat 7 (Beamish et al., 2020; Chen et al., 2021). This procedure resulted in 16 maxNDVI images, where images from 1999, 2000, 2003, 2007, 2009, 2010, and 2012 were available from Landsat 7, images from 2015, 2017 and 2018 were available from Landsat 8 and images from 2014, 2016 and 2019 were available from both Landsat 7 and 8. In the latter case, the untransformed Landsat 7 data were used for analysis (see Section 2.3.1–2.3.2).

For comparison between very high and moderate resolution NDVI products, three additional Landsat NDVI images of the study area were selected for dates closest to the acquisition dates of the very high resolution NDVI images (19 August 2010, 10 July 2015 and 1 August 2019), with a difference of at most 3 days. These images were all derived from Landsat 7 and underwent the same processing as described for the images used to derive annual maxNDVI series. For early 1 August 2019, an additional single Sentinel-2 MSI Level-2A image (10 m resolution) was obtained from Google Earth Engine (Gorelick et al., 2017). The image was atmospherically corrected using the Sen2Cor algorithm to derive surface reflectance and cloud-masked using the QA60 cloud mask band (Main-Knorn et al., 2017).

2.2.4. Weather Data & Thematic Map Data

Daily average temperature, precipitation and snow depth data from 1999 until 2019 were retrieved for the Chokurdakh weather station, located 27 km from the study site (WMO station code: 21946) from the AISORI database (<http://aisori-m.meteo.ru/waisori/>) of the All-Russia Research Institute of Hydrometeorological Information – World Data Center (RIHMI-WDC, 2020). All selected years (1999–2019) had at least 95% of complete daily data (346 days). For each year the average early summer temperature and total early summer precipitation (June 1st – August 5th) were calculated. Winter temperature was calculated as the average temperature between October 1st and April 31st. Maximum snow depth was calculated per winter season over the same period. We calculated the monthly Standardized Precipitation-Evapotranspiration Index (Vicente-Serrano et al., 2010) over a 12-month window (SPEI-12) as a measure of long-term moisture deficit or excess. SPEI was calculated using the spei package in R (Beguería et al., 2017) based on Hargreaves potential evapotranspiration. We used the mean

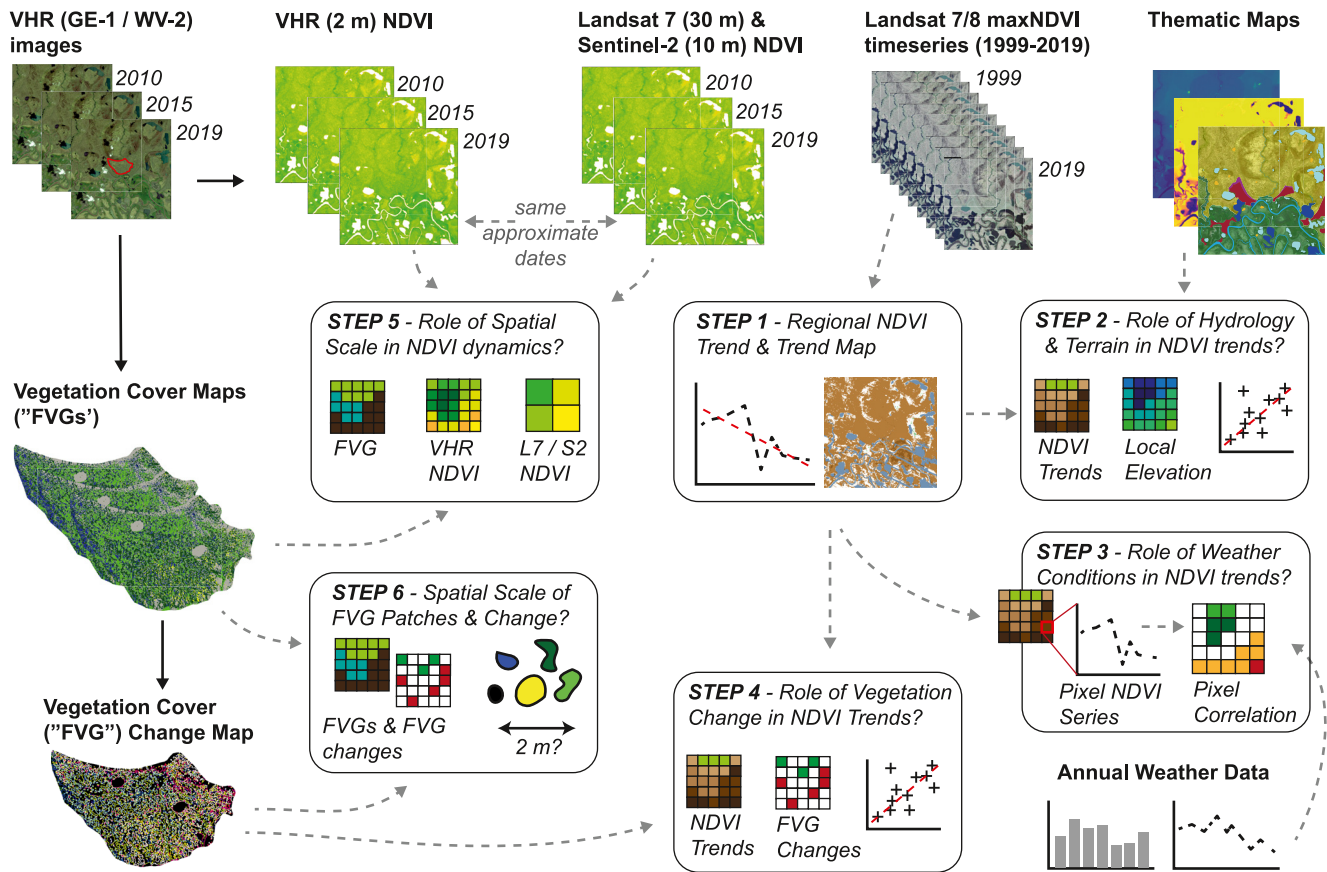


Figure 2. Workflow. **Step 1** - We quantified NDVI trends in the study area using a time series of peak summer maxNDVI Landsat images (paragraph 2.3.1). **Step 2** - We compared maxNDVI trends among geomorphological units, over elevation gradients and over a surface water occurrence gradient, to derive relations between NDVI dynamics, terrain and hydrology (paragraph 2.3.2). **Step 3** - We compared pixel maxNDVI trends with annual weather data to assess relations between NDVI trends and weather extremes, and spatial patterns therein (paragraph 2.3.2). **Step 4** - We compared maxNDVI trends with changes in higher resolution multitemporal vegetation maps to derive relations between NDVI trends and vegetation shifts (paragraph 2.3.3). Lastly, we compare NDVI data from image material of various resolution with high resolution land cover change maps (**Step 5**, paragraph 2.3.3) and spatial dimension of vegetation units and changes (**Step 6**, paragraph 2.3.3) to assess the role of spatial resolution in NDVI dynamics.

SPEI-12 of June and July as a measure of summer drought. In addition, we obtained a timeseries (1999–2019) of topsoil (top 7 cm) volumetric moisture content for a 10 by 10 km pixel containing the Chokurdakh Scientific Tundra station as derived from EUMETSAT scatterometer data (HSAF, 2020). Similar to weather variables, we calculated mean early summer (June 1st to August 5th) topsoil volumetric moisture content per year.

Existing thematic maps were used to characterize local hydrology, geomorphology and topography. We used the Global Surface Water Map (GSWM) (Pekel et al., 2016) to characterize local hydrology. From the GSWM, we extracted water occurrence data (Figure 1d) based on the Landsat record for the study area, indicating the percentage of years between 1999 and 2019 for which surface water was detected for a given Landsat pixel (Pekel et al., 2016). We used the 2 m spatial resolution ArcticDEM digital elevation model (Figure 1f) (Porter et al., 2018) to characterize local topography. We used a geomorphological map of the study area (Figure 1e) (Van Huissteden & Belelli Marchesini, 2014) to represent the spatial distribution of various landforms (e.g., floodplains, drained thaw lakes basins and Yedoma plateaus).

2.3. Statistical Analysis

2.3.1. Landsat NDVI Trend

We used Theil-Sen regression (Sen, 1968; Theil, 1950) to determine the decadal trend in annual mean maxNDVI for the study area as well as maxNDVI trends for individual pixels (Figure 2, step 1). Theil-Sen regression is a popular metric for NDVI trend analysis in Arctic regions (Lara et al., 2018; Myers-Smith et al., 2020; Nitze &

Grosse, 2016; Raynolds & Walker, 2016) due to its relative insensitivity to outliers (Fernandes & Leblanc, 2005). We performed Theil-Sen regression on the mean area annual maxNDVI as well as individual pixels' annual maxNDVI. In cases where both a Landsat 7 and Landsat 8 scene were available, the Landsat 7 scene was selected to avoid pseudoreplication and use of linearly transformed data. Pixels with less than 10 years' worth of data were considered inadequate for trend analysis and omitted (Forkel et al., 2013). Individual pixels' maxNDVI trends were visualized as maps. We used the *mblm* R package (Komsta & Komsta, 2013) to perform Theil-Sen regression.

2.3.2. Relation of Landsat NDVI Trends, Weather Events, Hydrological Dynamics and Landscape

We quantified the proportion of variance in pixel maxNDVI trends explained by geomorphological unit, elevation and water occurrence (Figures 1d–1f) using the coefficient of determination (R^2) (Figure 2, step 2). For association between raster values and categorical data (geomorphological unit), we report adjusted R^2 based on analysis of variance (ANOVA). For association between two raster datasets we use squared Pearson correlation. To assess significance of correlation between two raster datasets while accounting for spatial autocorrelation, we used Dutilleul's modified t -test (Clifford et al., 1989; Dutilleul et al., 1993; Fortin & Payette, 2002). We based Dutilleul's modified t -test on a random subsample representing 10% of the total amount of maxNDVI trend pixels (without replacement) to reduce computational demand. No significance was assessed for association between raster values and categorical data. Dutilleul's modified t -test was implemented using the *SpatialPack* (Osorio et al., 2020) and *SpatialEco* (Evans & Ram, 2021) packages in R.

To assess the degree to which maxNDVI dynamics in the study area are associated with recent dynamics of temperature, precipitation and hydrology, we compared annual maxNDVI values per pixel with annual summer temperature, summer precipitation, winter temperature, winter snow height and scatterometer-derived topsoil moisture (Section 2.2.4) using Spearman's correlation coefficient (ρ) to account for small sample sizes (Figure 2, step 3). We report mean and standard deviation of individual pixel's ρ^2 for each weather variable considered. Also here, we used the Landsat 7 scenes for years for which both Landsat 7 and Landsat 8 scene were available to avoid pseudoreplication. In addition, we computed correlation coefficients between individual pixels residuals relative to the Theil-Sen trend of the study area and linearly detrended weather variables. This way we assess to what degree local correlations result from synchronicity in trends (raw data correlations) or from synchronicity in year-to-year dynamics (detrended correlation analysis) (Bhatt et al., 2013; Box et al., 2019). Pixels with less than 10 years of maxNDVI values were excluded. To assess spatial patterns in pixel correlation coefficients among maxNDVI and weather variables, results were visualized as maps of raw and detrended correlation coefficients.

2.3.3. Relation of Landsat NDVI Trends to Vegetation Dynamics

To assess how a change in cover of different FVGs may affect NDVI trends, we compared Landsat maxNDVI trends with changes in FVG composition between 2010 and 2019 as derived from the FVG maps (Section 2.2.2). For this purpose, we repeated the Theil-Sen trend analysis (paragraph 2.3.1) within the focus study area (Figure 1c) for the period 2010–2019 to match the period and extent of the FVG maps. We then compared net changes per FVG within each Landsat trend pixel to the pixel's Theil-Sen slope using Pearson correlation and report R^2 (Figure 2, step 4). We report significance of correlations between FVG cover change and maxNDVI trends while accounting for spatial autocorrelation using Dutilleul's modified t -test.

To assess variability in NDVI among FVGs (Figure 2, step 5) we extract VHR NDVI values for each unique FVG in each year (2010, 2015, 2019) and present these as violin plots. The FVG maps (0.5 m resolution) were aggregated to a spatial resolution of 2 by 2 m to match the spatial resolution of the VHR NDVI images. We restricted this analysis to only include 2 by 2 m pixels where the FVG maps showed uniform vegetation pixels (i.e., all aggregated pixels belonged to the same FVG) and an average spectral class probability of 90% or more, based on initial random forest classification of the FVG maps. The VHR NDVI maps (Table S1 in Supporting Information S1) are based on the same VHR images that were used to classify the FVG maps (Magnússon et al., 2021) and relations between FVG and NDVI can therefore be expected. The violin plots are used to support comparison of relations between NDVI and FVG across spatial scales and years.

To assess whether relations between FVG composition and NDVI scale up from very high to moderate resolution (Figure 2, step 5), we compared NDVI of Landsat and Sentinel pixels to within-pixel FVG composition. We used the individual Landsat/Sentinel images that were collected at the same time as the VHR images that were used to generate the FVG maps (Section 2.2.3). For each Landsat/Sentinel image, we selected pixels within the smaller subsite (Figure 1c) and calculated the fractional cover of the different FVGs from the corresponding FVG map

within the larger Landsat/Sentinel pixels. We selected pixels with increasing fractional cover classes (0%, 10%, 25%, 50%, 75%, and 100%) for each FVG, with a maximum deviation of 5%. To avoid confounding effects of presence of other FVGs, we selected only those pixels for which fractional cover of the remaining FVGs in the pixels was proportional to the mean FVG composition of all pixels, also with a maximum deviation of 5% from the average FVG proportion of remaining classes per pixel. For each of the resulting series, we visualized NDVI against the increasing fractional cover for each FVG.

Lastly, we used the FVG maps to compute typical spatial scales of vegetation patches (Figure 2, step 6). We calculated the mean patch size of each of the six tundra vegetation classes from the FVG maps using the Landscapemetrics R package (Hesselbarth et al., 2019). We additionally calculated the mean patch size of areas that showed a change in FVG from 2010 to 2019 (i.e., adjacent pixels that show the same FVG transition). We compared these statistics to the spatial resolution of the various NDVI products used in this study. Using these statistical and visual comparisons, we assessed to what extent vegetation shifts and thermokarst dynamics on a subdecadal timescale may have affected NDVI dynamics at various spatial resolutions.

Our workflow is summarized in Figure 2.

3. Results

3.1. Landsat maxNDVI Trend

For the pixels with sufficient years (at least 10) of valid observations (85% of all pixels), an average maxNDVI trend of -0.0039 NDVI units per year was found. Of these pixels, the majority (76.28%) showed significant ($p < 0.05$) browning, and 4.64% of significantly browning pixels showed browning rates stronger than -0.01 NDVI units per year. Significant greening was found only in less than 1% of pixels, with the remaining 23.64% showing no significant trend. Temporal dynamics of mean maxNDVI of the study site show a trend break, with maxNDVI decreasing rapidly between 2007 and 2010 (Figure 3a). After a moderate increase between 2010 and 2012, maxNDVI steadily decreases again afterward. These dynamics were visible across the main geomorphological units in the area (Floodplains, Yedoma plateaus and Drained thaw lake basins). However, floodplains showed an especially pronounced dip in maxNDVI in 2017 (Figure S4 in Supporting Information S1), likely in response to early summer floods following extreme winter snowfall in 2016–2018 (see individual years' weather data in Table S2, Figure S2 in Supporting Information S1).

Although browning is ubiquitous across the landscape, some differences in magnitude are evident across elevation, geomorphological units and areas with different inundation frequency (Figures 3c–3e). Floodplain areas adjacent to the river Berelekh show the strongest browning trends within the study area (Figures 3b and 3e), consistent with stronger browning in areas with more frequent water occurrence, as evident from the Global Surface Water Map (Figure 3d). Lower elevation areas along the inner edges of drained thaw lake basins tend to show no trend in maxNDVI, and occasionally show local greening (Figure 3b). Overall, these results indicate rather uniform browning dynamics from 1999 to 2019 across the landscape, but relatively rapid browning of periodically inundated floodplains and little browning and occasional greening in low elevation margins of drained thaw lake basins.

3.2. Effect Vegetation Compositional Changes on NDVI

We compared pixel Landsat maxNDVI trends to FVG cover changes between 2010 and 2019 within the same Landsat pixel area based on high resolution vegetation maps. We found that changes in cover of several FVGs are significantly associated with NDVI trends, but that the proportion of variance in maxNDVI trends explained by such vegetation changes is very small (R^2 of up to 0.040) (Figure 4). Changes in shrub and sedge cover within a Landsat pixel were not significantly related to maxNDVI trends. Pixels with increases in lichen cover or open water cover showed a tendency ($p < 0.1$) of stronger browning. Changes in *Sphagnum* and tussock cover explained a significant amount of variation in maxNDVI trends ($R^2 = 0.040$ and $R^2 = 0.026$, respectively). Increased tussock cover was associated with higher values of maxNDVI trends (less browning or occasionally greening), while increased *Sphagnum* cover was associated with lower values of maxNDVI trends (more browning).

Comparison of individual FVG maps (2010, 2015, and 2019) with various NDVI products with similar acquisition dates indicates a similar pattern of association between FVGs and NDVI values (Figure 5). Landsat or Sentinel pixels with higher *Sphagnum* cover generally show lower NDVI, while pixels with higher tussock cover

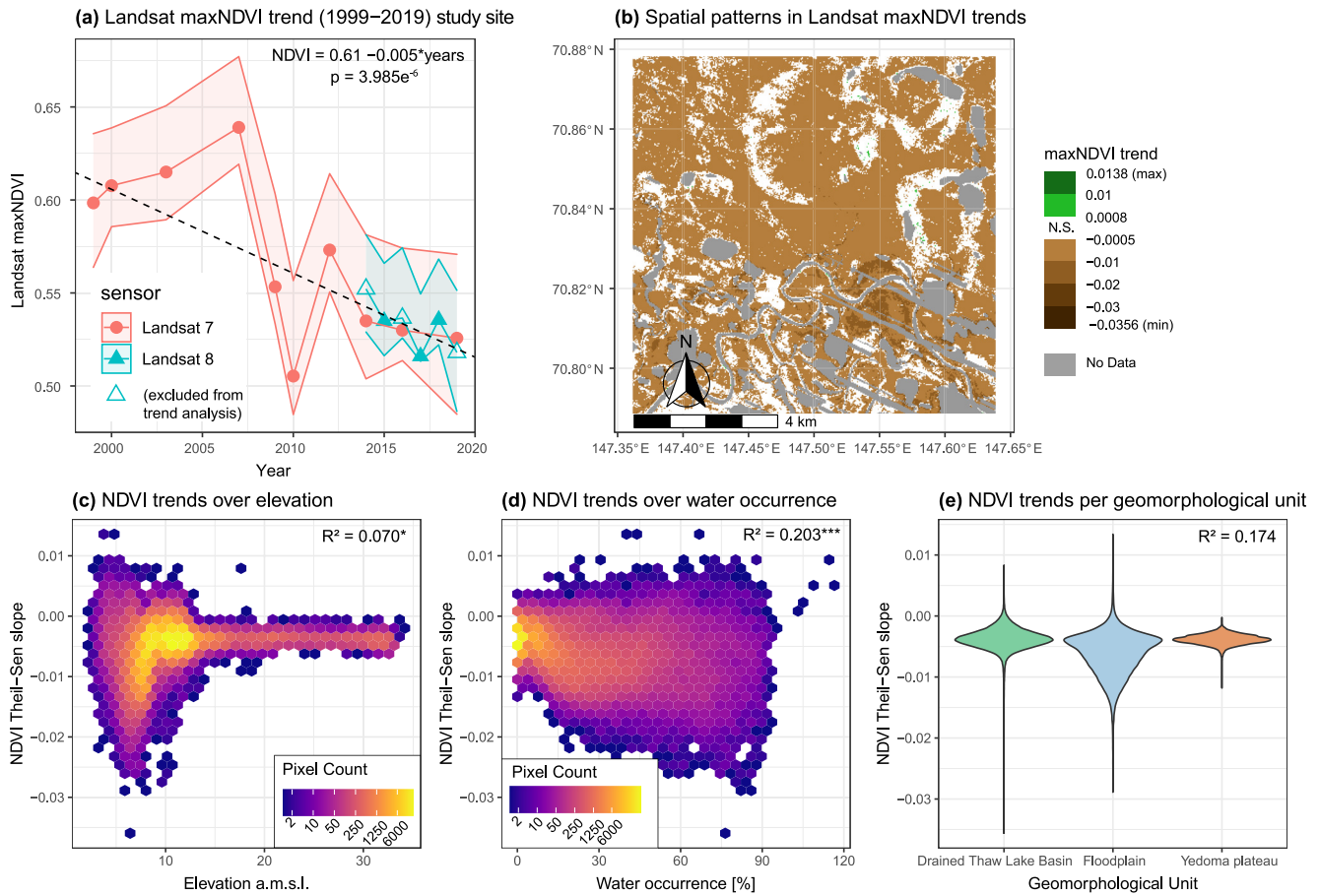


Figure 3. Observed Landsat maxNDVI Trends and variability across elevation, water occurrence frequency and geomorphology. (a) Mean (point) and interquartile range (shaded area) of maxNDVI for the years during which cloud free Landsat images were available during the peak growing season (July 20th to August 5th). Landsat 8 values (blue) were corrected for discrepancies between Landsat 7 and Landsat 8 sensors based on a linear fit. Dashed line and text show Theil-Sen trend ($n = 13$). Note that in years for which both a Landsat 7 and Landsat eight image were available, only the Landsat seven image was used for trend analysis (see paragraph 2.3.1). Unused Landsat 8 scenes are visualized as open triangles. (b) Map of pixel maxNDVI Theil-Sen trends. Gray areas had less than 10 years of NDVI data and were omitted from trend analysis. Brown pixels are significantly browning, white pixels showed no significant trend ($p > 0.05$), green pixels show significant greening. (c) Hexagonal binned heatmap of the amount of pixels falling in a particular range of elevation (ArcticDEM) and maxNDVI trends. Color scale is logarithmic. (d) Hexagonal binned heatmap of the amount of pixels falling in a particular range of water occurrence probability (Global Surface Water Map) and maxNDVI trends. Color scale is logarithmic. (e) maxNDVI trends per geomorphological unit. Violin width is proportional to the probability of observing a trend of a particular magnitude within that class. Geomorphological unit. N.S. = not significant, + = $p < 0.1$, * = $p < 0.05$, ** = $p < 0.01$, *** = $p < 0.001$. p values for (d) and (e) were generated based on Dutilleul's modified t -test.

show higher NDVI (Figures 5a–5d). The areal cover of open water features and lichen vegetation within a Landsat or Sentinel pixel is generally too low to estimate the effect of increasing lichen and open water cover within a single Landsat or Sentinel NDVI image (Figures 5a–5d). Interestingly, increasing pixel shrub cover is associated with higher NDVI values in Landsat and WorldView-2 images from 2015 (Figures 5b and 5f), but not in images from 2019 (Figure 5c,5d,5g).

Vegetation class transitions based on the FVG maps (2010–2019) show that local vegetation compositional changes in the focus area typically occur on small spatial scales (mean = 5 m^2 , 90% CI = $0.25\text{--}19.5 \text{ m}^2$, Figure 5h) compared to the resolution of Sentinel and Landsat data. Vegetation functional groups that showed significant (but weak) association with local magnitude of NDVI trends (*Sphagnum*, tussock sedge) generally covered a relatively large proportion of the study area and showed relatively large changes in cover over 2010 to 2019 (Table S3 in Supporting Information S1). In case of *Sphagnum*, typical NDVI ranges are relatively distinct from other vegetation types (Figures 5e–5g). Vegetation functional groups that showed no significant association with local NDVI trends generally showed small areal cover and changes to and from these classes affected a small proportion of the focus area (Table S3 in Supporting Information S1). Although local shifts from shrub to open

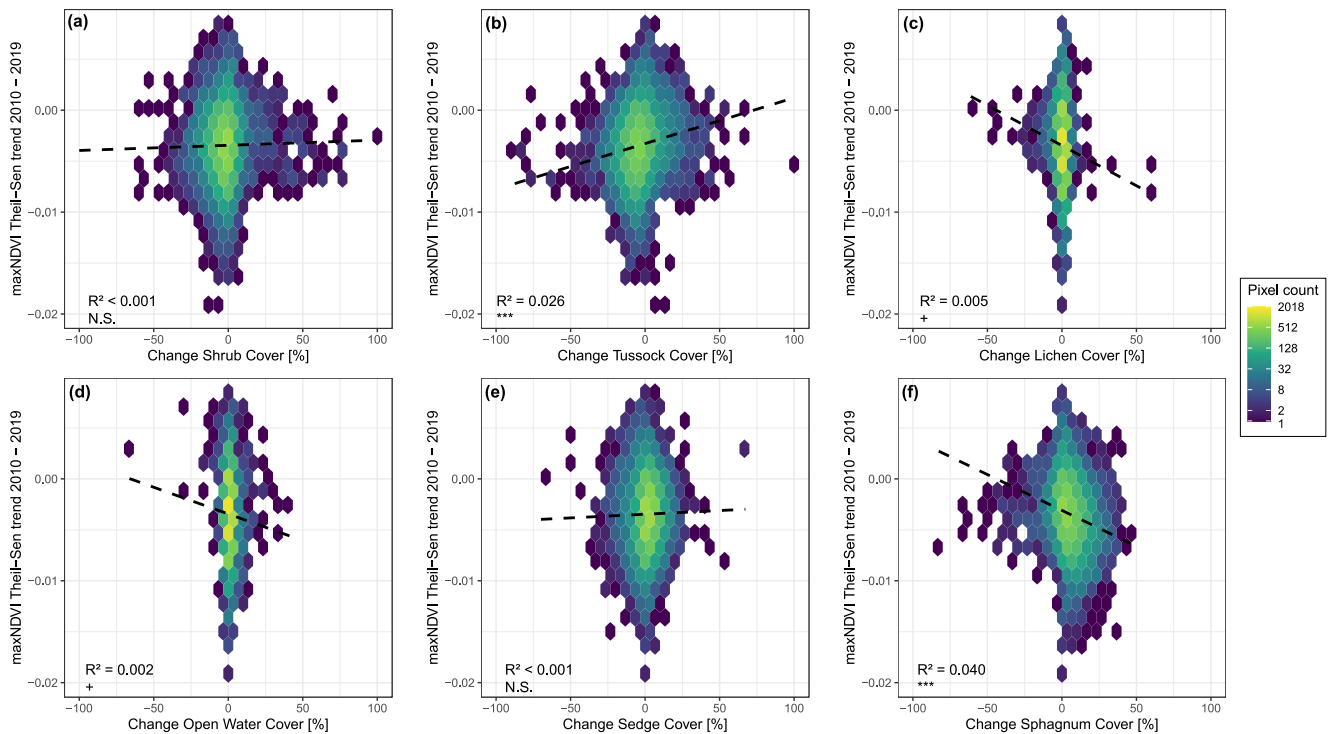


Figure 4. Relation between Landsat maxNDVI trend over 2010 – 2019 and change in cover of (a) shrub, (b), tussock sedge, (c) lichen, (d) open water, (e) sedge and (f) Sphagnum vegetation, as derived from high resolution classified satellite images over the same period. Scatter plots are visualized as hexagonal binned heatmaps with logarithmic color scale, where color indicates the number of pixels that fall within a particular range of vegetation cover change and maxNDVI trends. Text labels indicate R^2 based on Pearson's R for a linear fit. N.S. = not significant, + = $p < 0.1$, * = $p < 0.05$, ** = $p < 0.01$, *** = $p < 0.001$ (based on p values corrected for spatial autocorrelation using Dutilleul's modified t-test).

water due to thermokarst may manifest on relatively large areas ($\pm 15 \text{ m}^2$ on average) (Table S3 in Supporting Information S1) and would be expected to result in lower NDVI (Figures 5e–5g), changes in open water area had little impact on NDVI trends (Figure 4d).

3.3. Association of NDVI With Weather Variables

NDVI dynamics from 1999 to 2019 show spatially consistent patterns of association with snow dynamics, soil moisture and summer precipitation (Figure 6). Less than 5% of available pixels (with >10 maxNDVI observations) showed significant correlation of annual maxNDVI with summer temperature and summer SPEI-12 (Figures 6a and 6e, Table 1). This is less than might be expected due to chance with a significance criterion of $\alpha = 0.05$. A substantial portion of available pixels showed significant positive correlation of annual maxNDVI with summer precipitation, and significant negative correlation with snow height (Figures 6b and 6c, Table 1). Around 10% of available pixels showed negative association with winter temperature and positive association with summer soil moisture (Figures 6d and 6f, Table 1). As warm winters and winters with a lot of snow generally coincide (Table S2 in Supporting Information S1), negative correlations with snow height and winter temperatures may reflect the same dynamic. Of all annual climate variables, snow height ($\rho = -0.621$, $p = 0.023$, $n = 13$), summer precipitation ($\rho = 0.536$, $p = 0.059$, $n = 13$), and topsoil moisture ($\rho = 0.533$, $p = 0.064$, $n = 13$) also showed the strongest association with average annual maxNDVI of the entire study area (Figure S2 in Supporting Information S1). To assess to what extent association may occur due to synchronous trends in NDVI and weather variables, or due to similarity in year-to-year dynamics, we additionally performed detrended correlation analysis. Here, associations of NDVI and weather variables are less pronounced (Figure S3 in Supporting Information S1), and only summer precipitation, snow height and winter temperature show localized association of year-to-year variability (Figure 6, Table 1). This suggests that associations of NDVI with weather conditions mainly reflect synchronous trends of browning, warming winters and recent snowfall extremes and dry summers, but that year-to-year weather variability additionally affects NDVI on local scales.

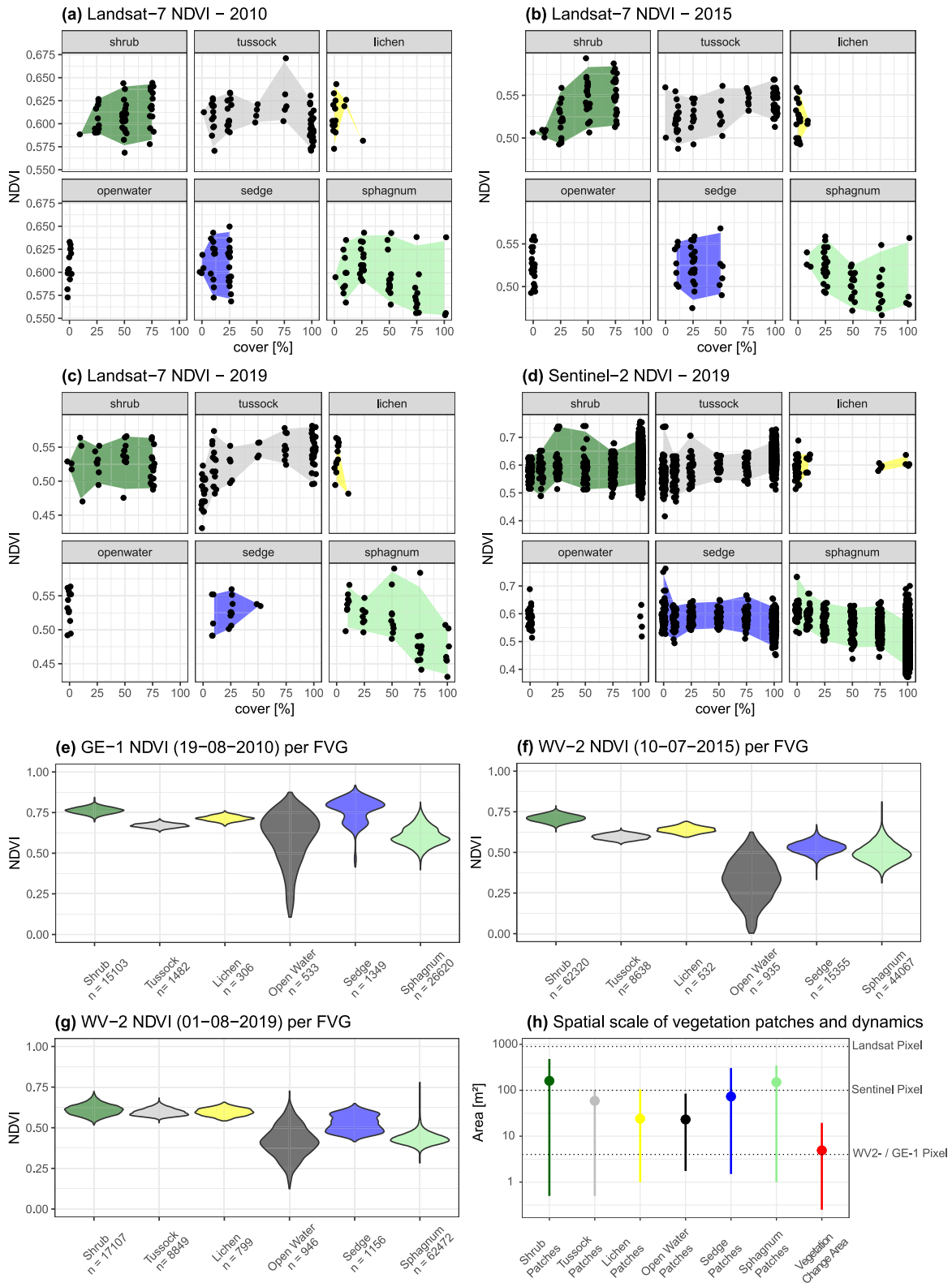


Figure 5.

NDVI—weather data associations show distinct spatial patterns (Figure 6). Positive associations of annual maxNDVI with summer precipitation and topsoil moisture are mostly evident in higher elevation sites outside floodplains (Figures 6b and 6f). Negative associations of annual maxNDVI with snow height and winter temperature are stronger both in lower elevation floodplains and in higher elevation Yedoma plateaus (Figures 6c and 6d). Slightly elevated (Figure 1f) edges and centers of drained thaw lake basins show stronger association with snow height than lower parts of drained thaw lake basins (Figure 6d). Detrended correlation analysis indicates that years with relatively low summer rainfall and high snow accumulation are associated with locally positive NDVI residuals in low elevation inner margins of drained thaw lake basins, but relatively low NDVI in floodplains (Figures 6h and 6i). These trends indicate that sensitivity of tundra NDVI to precipitation varies throughout the landscape on sub-kilometer scale, with small topographic contrasts (range of meters to approximately 25 m, Figure 1f) already affecting NDVI response to extreme snowfall and drought.

4. Discussion

With this study, we set out to assess whether recent browning of the Indigirka Lowlands could be explained by weather dynamics (particularly recent heatwaves and drought), floods and small-scale vegetation shifts related to thermokarst. Of all potential mechanisms, browning appeared most strongly associated with precipitation dynamics. Below, we will first discuss how browning dynamics identified in this study relate to previous findings of tundra browning. Then we will discuss the influence, spatial scale and dynamics of the different phenomena that we found to be associated with browning (recent summer drought, flood events and thermokarst-induced vegetation shifts). Finally, we discuss implications for the Indigirka Lowlands region and for future Arctic greening in general.

4.1. The Indigirka Lowlands in the Context of Panarctic NDVI Dynamics

With an areal mean maxNDVI trend of -0.0039 NDVI units per year and 76% of available pixels showing significant browning, we find strong and widespread browning for our study area compared to previously reported NDVI trends for the Indigirka Lowlands region or for the Arctic in general (Berner et al., 2020; Frost, Macander, et al., 2021; Myers-Smith et al., 2020; National Academies of Sciences and Medicine, 2019; Magnússon et al., 2021; Mekonnen et al., 2021). On a panarctic scale, Landsat NDVI generally shows positive associations with summer warming in recent decades (Berner et al., 2020), which is in contrast with our results (Figures 6a and 6g). Instead, we identified spatially variable associations of NDVI with moisture dynamics (most notably summer precipitation and snow depth) (Figure 6), in line with earlier findings of topographical and regional variability in precipitation—NDVI relations (Berner et al., 2020; Frost, Bhatt, et al., 2021; Lara et al., 2018).

On a panarctic level, greening is more evident in upland regions with temperatures increases as long as moisture availability is not limited, while browning is more evident in lowland regions that show a drying trend (Berner et al., 2020). In the relatively warm and strongly maritime Yukon-Kuskokwim delta, Frost, Bhatt, et al. (2021) found positive associations of various NDVI products with summer temperature, whereas relations with summer precipitation were absent or even negative for lowland sites. However, in relatively arid Northern Alaskan regions, Chen et al. (2021) found strong dependence of NDVI on soil moisture and precipitation variables. Lara et al. (2018) found that the response of Landsat NDVI to year-round temperatures and precipitation varies among geomorphological subunits, with particularly negative responses to precipitation increases and positive responses to temperature increases in wet sites such as tundra ponds. Consistent with its relatively dry continental climate (Fujinami et al., 2016), our study region shows low NDVI during dry summers (2010, 2018, and 2019, Figure 3a,

Figure 5. Relation of vegetation composition and NDVI across spatial scales within the focus area. (a) Relation of Landsat NDVI and vegetation composition for the FVG map for 19-08-2010 and a Landsat 7 NDVI image close to the same date (22-08-2010). (b) Relation of Landsat NDVI and vegetation composition for the FVG map for 10-07-2015 and a Landsat 7 NDVI image close to the same date (12-08-2015). (c) Relation of Landsat NDVI and vegetation composition for the FVG map for 01-08-2019 and a Landsat 7 NDVI image on the same date (01-08-2019). (d) Relation of Sentinel NDVI and vegetation composition for the FVG map for 01-08-2019 and a Sentinel 2 NDVI image on the same date (01-08-2019). For figures (a)–(d), pixels were selected with increasing cover of each of the FVGs and filtered for representative proportional cover of the remaining FVGs. Shaded areas represent a 90% confidence interval of NDVI values for each cover value. (e) GeoEye-1 NDVI per FVG, both based on the 2010 GeoEye-1 image (19-08-2010, Table S1 in Supporting Information S1). (f) WorldView-2 NDVI per FVG, both based on the 2015 WorldView-2 image (10-07-2015, Table S1 in Supporting Information S1). (g) WorldView-2 NDVI per FVG, both based on the 2019 WorldView-2 image (01-08-2019, Table S1 in Supporting Information S1). For (e)–(g), only pixels with >90% spectral classification probability were selected. (h) Median and 90%–CI of patch size per FVG (based on the 2015 FVG map) and area of FVG change from 2010 to 2019, relative to the approximate area of a GeoEye-1/WorldView-2 pixel, Sentinel-2 pixel and Landsat pixel.

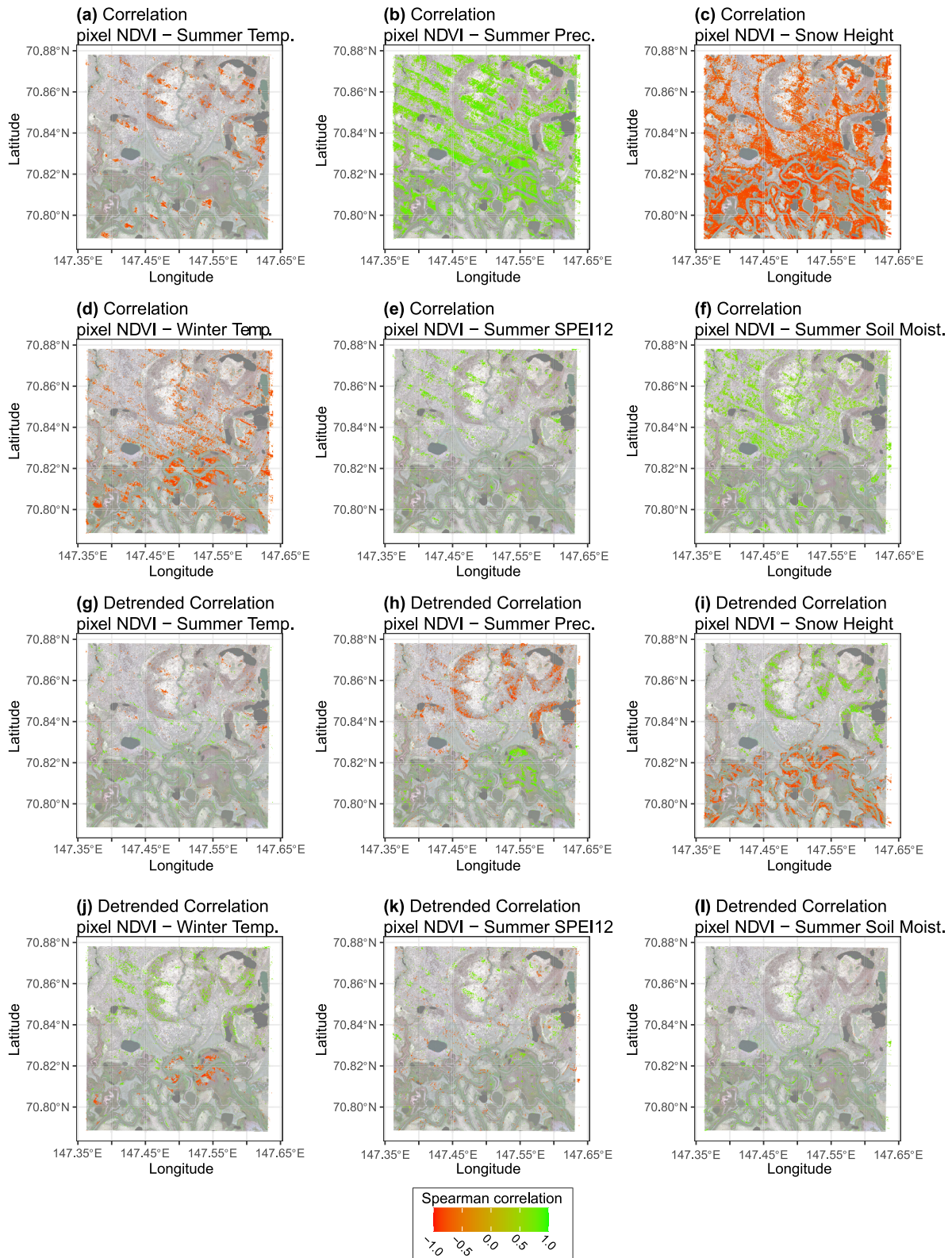


Figure 6.

Table 1

Summary of Correlation and Detrended Correlation Analysis of Individual Pixel Annual maxNDVI and Weather Variables

Weather variable	Correlation analysis			Detrended correlation analysis		
	% of pixels significant	Mean ρ (st. dev.) ^a	Mean ρ^2 (st. dev.) ^b	% of pixels significant	Mean ρ (st. dev.) ^a	Mean ρ^2 (st. dev.) ^b
Summer temperature	3.68	−0.15 (0.26)	0.09 (0.11)	2.21	−0.01 (0.28)	0.08 (0.10)
Summer precipitation	28.57	0.43 (0.25)	0.25 (0.19)	6.87	−0.06 (0.4)	0.12 (0.14)
Snow height	39.62	−0.50 (0.25)	0.31 (0.21)	9.83	−0.01 (0.36)	0.13 (0.16)
Winter temperature	9.91	−0.34 (0.23)	0.17 (0.15)	5.18	0.15 (0.29)	0.11 (0.13)
Summer SPEI-12	4.06	0.21 (0.23)	0.10 (0.12)	3.27	0.01 (0.30)	0.09 (0.11)
Summer topsoil moisture	11.44	0.36 (0.21)	0.17 (0.14)	2.44	0.15 (0.28)	0.08 (0.10)

^aAverage Spearman correlation coefficient (ρ) over all available pixels, with standard deviation in brackets. ^bAverage coefficient of determination (ρ^2) over all available pixels, with standard deviation in brackets.

Figure S1 in Supporting Information S1) and positive association of NDVI with summer precipitation and soil moisture, particularly on elevated Yedoma plateaus (Figures 6b and 6f). Local patterns in detrended correlation emphasize such patterns in precipitation—NDVI associations across hydrological and topographical gradients (Figure 6). This suggests a strong role of baseline moisture availability in the response of tundra NDVI to annual temperature and moisture availability, governed both by regional climate and local topography.

4.2. Association of NDVI With Weather Patterns and Hydrology

Recent floods induced by extreme snow accumulation have likely contributed strongly to the observed browning. Of all weather variables, snow depth displayed the strongest overall raw correlation with mean annual maxNDVI (Figure S2 in Supporting Information S1). High snow accumulation led to extensive floods throughout the Indigirka Lowlands in 2016–2018 and strong browning surrounding the Khroma and Indigirka rivers (Magnússon et al., 2021; Tei et al., 2020). Floods in 2017 and 2018 inundated the entire floodplain and parts of surrounding drained thaw lake basins (Van Huissteden et al., 2021; Magnússon & Heijmans, pers. obs.). Floodplains show record low NDVI in 2017 (Figure S4 in Supporting Information S1), strong browning compared to the rest of the study area (Figure 3b) and particularly negative association with snow depth (Figures 6c and 6i). This makes waterlogging in the early summer season a likely explanation for the particularly strong recent browning of the Indigirka Lowlands. This could be governed by direct waterlogging, by delayed or compromised plant growth or by depositional and erosional processes. Interestingly, the dry and warm year 2019 (Figure S1 in Supporting Information S1) showed a pronounced increase in NDVI in floodplains, while Yedoma plateaus and drained thaw lake basins continued browning (Figure S4 in Supporting Information S1). In addition, the few areas that showed greening or no significant change in maxNDVI were generally situated around lakes and in wet areas along the inner circumference of drained thaw lake basins (Figure 3b). This could be indicative of vegetation succession where aquatic species colonize lake margins (Roach et al., 2011; Troeva et al., 2010) and recently drained parts of thaw lakes (Morgenstern et al., 2013). This suggests that floodplains and connected lowland areas may have shown particularly strong browning due to flooding following extreme snowfall, but that such periodically inundated sites may also show rapid recovery of vegetation and NDVI.

Similarly, identified associations between summer rainfall and NDVI (Figures 6 and S2 in Supporting Information S1) may be strongly driven by recent extremes. Over the studied period (1999–2019), the study area

Figure 6. Association of annual maxNDVI values with annual weather data per Landsat maxNDVI trend pixels. Stripes are caused by scan line corrector failure in several of the Landsat 7 NDVI images (Storey et al., 2005). a–f shows Spearman Correlation of individual pixel's annual maxNDVI with (a) mean summer (June 1st to August 5th) temperature, (b) total summer (June 1st to August 5th) precipitation, (c) maximum winter (October 1st to April 31st) snow height, (d) mean winter (October 1st to April 31st) temperature, (e) mean summer (June–July) 12-month Standardized Precipitation–evapotranspiration Index (SPEI-12) and (f) mean summer (June 1st to August 5th) topsoil (0–7 cm) volumetric moisture content. g–l shows Spearman Correlation of individual pixel annual maxNDVI Theil–Sen residuals with (g) linearly detrended mean summer (June 1st to August 5th) temperature, (h) linearly detrended total summer (June 1st to August 5th) precipitation, (i) linearly detrended maximum winter (October 1st to April 31st) snow height, (j) linearly detrended mean winter (October 1st to April 31st) temperature, (k) linearly detrended mean summer (June–July) 12-month Standardized Precipitation–evapotranspiration Index (SPEI-12) and (l) linearly detrended mean summer (June 1st to August 5th) topsoil (0–7 cm) volumetric moisture content. In all panels, insignificant associations have been filtered out and are shown as transparent pixels. Basemap: 2019 WorldView-2 satellite image, © MAXAR, 2019.

shows distinct periods of low (2007–2010) and extremely high (2011) summer rainfall (Figure S1 in Supporting Information S1). 2019 and 2020 show anomalously high summer temperatures and extreme drought (Figure S1 in Supporting Information S1, Overland & Wang, 2021). We found that maxNDVI decreased particularly over the low rainfall period of 2007–2010 (Figure 3a) and increased temporarily following the high rainfall year 2011 (Table S2 in Supporting Information S1, Figure 3a, Figure S1 in Supporting Information S1). Although no causal inferences can be made based on this synchronicity, such temporal dynamics of NDVI and correlations between NDVI and weather variables support moisture limitation as a potential factor in tundra browning. This would be in line with recent findings of moisture-limitation of tundra productivity across the Arctic biome (Zona et al., 2022).

The negative response of maxNDVI to warm winters with high snow accumulation on Yedoma plateaus and other elevated sites (Figure 6c) was not supported by detrended correlations (Figure 6i) and likely reflects a mechanism other than flooding, as spring and early summer floods do not reach these elevated sites (Figure 1d, Heijmans, pers. obs.). Potential mechanisms could be delayed onset of the growing season or erosional processes (Van Huissteden et al., 2021). Years with record high snowfall generally also showed lower than average rainfall in summer and higher than average winter temperatures (Figure S2 in Supporting Information S1), which may have additionally contributed to low NDVI. Detailed field monitoring and experimentation (e.g., snowpack manipulation) would help clarify whether and why warmer winters with high snowfall seem associated with lower tundra NDVI in such upland sites.

4.3. Association of NDVI With Vegetation Dynamics

Only a small proportion of browning in this region could be explained by small-scale thermokarst and associated succession dynamics toward wetland vegetation (Figure 4). In a focus study area representing a single drained thaw lake basin, we found NDVI declines to be marginally stronger in locations with increasing cover of open water and *Sphagnum* vegetation and decreasing cover of mixed tussock sedge vegetation. Relatively high NDVI of tussock sedge vegetation (Loranty et al., 2011; Reynolds et al., 2019) and low NDVI for open water features and *Sphagnum* vegetation (Lin et al., 2012; Reynolds & Walker, 2016; Schubert et al., 2010) are consistent with such patterns. Despite high classification accuracy of individual vegetation maps (91%–93%), uncertainties in small scale vegetation change detection (Magnússon et al., 2021) may have contributed to weak associations. Observed recent increases in *Sphagnum* cover in the study area (Magnússon et al., 2021) may have contributed marginally to the observed browning trend.

In contrast with earlier research into relations of vegetation cover and NDVI (Blok, Schaepman-Strub, et al., 2011; Boelman et al., 2011; Forbes et al., 2010; Loranty et al., 2011), we find no consistent relation between shrub cover and NDVI (Figures 4 and 5). Instead, associations between shrub cover and NDVI differed over time. Earlier season images from 2015 (WorldView-2, July 10th and Landsat 7, July 12th) show stronger association of shrub cover with NDVI (Figures 5b and 5f). The very late summer GeoEye-1 image from 2010 (August 19th) (Figure 5e) shows relatively strong association between sedge vegetation cover and NDVI values compared to other years. Earlier work confirms that separability of tundra vegetation functional groups based on NDVI differs throughout the season (Karami et al., 2018). Alternatively, 2015 was a relatively wet summer compared to 2010 and 2019 (Figure S1 in Supporting Information S1). Shrub vegetation NDVI was particularly low in 2019 (Figure 5g), and field observations in this dry year (Figure S1 in Supporting Information S1) confirm a relatively high amount of standing dead shrubs (Magnússon & Heijmans, pers. obs.). This suggests that seasonal timing and moisture availability may affect relative NDVI values among tundra vegetation functional groups.

Contrary to our expectation, thermokarst dynamics explained very little variance in Landsat NDVI trends (Figure 4) (<1%). Formation of thaw ponds in shrub vegetation affected only 0.5% of the focus study area (Table S3 in Supporting Information S1) and is generally followed by colonization of sedge vegetation on subdecadal timescales (Magnússon et al., 2021). In addition, not all thaw ponds show low NDVI values in the very high resolution images (Figures 5e–5g), which may result from spectral mixing, presence of sparse vegetation cover or shallow depth (Grosse et al., 2008). This likely explains why thaw pond formation does not seem to significantly affect NDVI trends.

In general, we find an increasing degree of association between vegetation cover and NDVI (Figures 5a–5g) in smaller spatial resolution datasets, and variable impacts on NDVI associated with different vegetation change trajectories (Table S3 in Supporting Information S1) that manifest on small spatial scales (Figure 5h). This

suggests that capturing the effects of thermokarst and associated vegetation dynamics on NDVI at subdecadal timescales likely requires image material with high temporal availability and spatial resolution at least comparable to that of the WorldView-2 and GeoEye-1 dataset used here (2 m), but preferably smaller (e.g., drone data).

4.4. Implications for the Indigirka Lowlands Ecosystem

Our findings suggest that recent NDVI dynamics in this region are driven more by precipitation extremes and drought than by warming, implying that drought and increased future precipitation variability could promote further browning. Differential responses across topographical and hydrological gradients may induce increased spatial heterogeneity in browning rates, even in this relatively flat lowland ecosystem. Based on current IPCC scenarios of 1.5–4°C global warming, temperature increases of 3.7–9.6°C (1.9–6.0°C in June–August) and precipitation increases of 15%–38% (7.2%–14% in June–August) are predicted for the Russian Arctic (IPCC, 2021). Increased occurrence of heatwaves and increased interannual variability in precipitation is expected, with both dry periods and precipitation extremes increasing (IPCC, 2021; Wang et al., 2021). Warming air temperatures and increased occurrence of extreme precipitation may additionally promote permafrost degradation, thermokarst and vegetation disturbance in this ice-rich ecosystem (Biskaborn et al., 2019; Douglas et al., 2020; Magnússon et al., 2022; Nitzbon et al., 2020). While increases in heatwaves and precipitation are expected, there is still considerable uncertainty whether drought events will increase or decrease in the Russian Arctic and much of the polar regions (IPCC, 2021). Recent heatwaves and drought events have been attributed to complex interactions of anthropogenic warming, atmospheric teleconnection patterns and snow albedo feedbacks (Collow et al., 2022; Overland & Wang, 2021), which complicates prediction of such events in the future (Overland & Wang, 2021). Better quantification of relations between NDVI and drought as well as better forecasting of future drought spells would be necessary to assess risk of future tundra browning.

Our results suggest that, particularly in lowland ecosystems adjacent to major river systems, increased occurrence of tundra browning events may be expected as a result of flooding. Flooding frequency for Siberian rivers may increase by 2%–5%, with local increases of up to 10% for the Indigirka river (Shkolnik et al., 2018). This will likely result in further negative impacts on tundra NDVI, but also boreal forest growth, infrastructure (Tei et al., 2020) and nesting site availability for birds (Haverkamp et al., 2022). However, our results suggest that in river-adjacent tundra floodplains with graminoid, peat moss and willow vegetation, flood-induced decreases in NDVI may be short-lived if followed by drier, warm summers.

Thermokarst and associated highly localized vegetation shifts towards aquatic species such as sedges and *Sphagnum* at the expense of higher NDVI vegetation types appeared to contribute little to local browning, but likely require higher resolution data to be properly inventoried. Apart from impacts on NDVI, these processes have been observed to result in increased methane emissions and carbon source dynamics in Siberian tundra ecosystems (Beckebanze et al., 2022; Nauta et al., 2015). Their poor distinguishability in moderate resolution NDVI data (Figure 5) may lead to overestimation of carbon uptake by tundra vegetation (Beckebanze et al., 2022). Finally, our analysis was limited to a single drained thaw lake basin. Although such features occupy a large proportion of the North-Eastern Siberian tundra (Fedorov et al., 2018), vegetation dynamics and thermokarst activity may differ among landforms and stages of development of drained thaw lake basins (Jones et al., 2022; Jorgenson & Shur, 2007; Morgenstern et al., 2013; Zona et al., 2010).

5. Conclusions and Recommendations

Our remote sensing based study has provided preliminary insights into the mechanisms that might underlie the strong recent browning observed in the Indigirka Lowlands, despite a continued trend of overall Arctic greening. In this ice-rich, highly continental lowland tundra ecosystem, browning appeared to be driven strongly by moisture dynamics. Low NDVI was observed both in summer with low rainfall and in summers with extensive flooding due to high snowfall. Small-scale vegetation shifts and thermokarst processes explained only little variance in Landsat NDVI trends. To better understand whether such processes may induce tundra browning in the future in other Arctic regions, the following remaining knowledge gaps should be addressed:

While drought and extreme snowfall seem associated with browning in this ecosystem in recent years, we cannot draw robust conclusions about causality or magnitude of effects of precipitation extremes on tundra NDVI based on the present correlative study. Instead, we hope this study provides direction for future research of causes of

tundra browning. Better understanding potential climatic drivers of recent and rapid tundra browning in the Indigirka Lowlands will benefit from longer-term Landsat NDVI monitoring. Additionally, time-integrated NDVI may reflect climate-growth associations better than maximum growing season NDVI (Bhatt et al., 2013), although the sparse availability of Landsat scenes does not currently allow for reliable quantification of time-integrated NDVI. Experimental studies will be necessary to provide causal evidence for climate—NDVI relations, potentially with different treatment levels differentiating gradual changes from extreme events. Long-term monitoring following experimental studies is essential to capture recovery dynamics and duration of browning events. The fact that the recent climate record for our site has shown both periods of dry heatwaves, extreme snowfall and floods and extreme rainfall within a period of only 10 years suggests that simulation of multiple, consecutive extremes may be a valuable addition to simulate a rapidly changing Arctic.

To assess the degree to which NDVI dynamics are indicative of highly localized and spatially variable processes such as thermokarst and changes in vegetation composition and properties, a multi-scale approach is likely necessary (Myers-Smith et al., 2020). For our ecosystem, NDVI products with spatial resolutions of at most 2 m but preferably less seem to be appropriate given the spatial dimensions on which vegetation changes manifest on timescales of approximately 10 years. This likely differs among ecosystems. Comparison of localized NDVI-impacts with coarser resolution NDVI timeseries that are typically used for monitoring (e.g., Landsat and, with increasing temporal availability, Sentinel data) may indicate how and on what timescales such small scale changes on the ground propagate to larger spatial scales. Increasing availability of very high resolution image products and drone technology opens up the possibility of strategically repeated acquisition of high resolution NDVI data for comparison with field-measured changes and longer-term, coarser resolution NDVI timeseries. Although naturally occurring vegetation shifts remain a key process to monitor, a potentially strategic way to quickly gain insight into the effect of tundra vegetation changes on NDVI may be monitoring of multi-resolution NDVI under targeted removal of particular plant functional groups on various spatial scales. Lastly, with respect to impacts of vegetation composition and properties on NDVI, collection of multiple NDVI data points per season would likely also allow better assessment of the contribution of different vegetation groups to changes in NDVI.

Conflict of Interest

The authors declare no conflicts of interest relevant to this study.

Data Availability Statement

This study used openly available existing data, except for very high resolution commercial satellite images, which were obtained from MAXAR under a copyright license for internal use and are not accessible to the public or research community. Table S1 in Supporting Information S1 lists product specifications for acquisition of these satellite images. Landsat images used to derive NDVI trends are available from Google Earth Engine (Gorelick et al., 2017). Weather data for the Chokurdakh weather station (WMO station code: 21946) are available from the All-Russia Research Institute of Hydrometeorological Information - World Data Centre (RIHMI-WDC, 2020). Soil moisture scatterometer data are available from EUMETSAT (HSAF, 2020, datasets H141, H142). Surface water recurrence data are available from Pekel et al. (2016). The ArcticDEM digital elevation model is available from Porter et al. (2018). The geomorphological map is available from PANGAEA, see Van Huissteden and Beletti Marchesini (2014). Multitemporal very high resolution vegetation maps are available from the DANS EASY repository (Magnússon et al., 2021).

References

- Abbott, B. W., Jones, J. B., Schuur, E. A., Chapin, F. S., III, Bowden, W. B., Bret-Harte, M. S., et al. (2016). Biomass offsets little or none of permafrost carbon release from soils, streams, and wildfire: An expert assessment. *Environmental Research Letters*, 11(3), 034014. <https://doi.org/10.1088/1748-9326/11/3/034014>
- Beamish, A., Reynolds, M. K., Epstein, H., Frost, G. V., Macander, M. J., Bergstedt, H., et al. (2020). Recent trends and remaining challenges for optical remote sensing of arctic tundra vegetation: A review and outlook. *Remote Sensing of Environment*, 246, 111872. <https://doi.org/10.1016/j.rse.2020.111872>
- Beckebanze, L., Rehder, Z., Holl, D., Wille, C., Mirbach, C., & Kutzbach, L. (2022). Ignoring carbon emissions from thermokarst ponds results in overestimation of tundra net carbon uptake. *Biogeosciences*, 19(4), 1225–1244. <https://doi.org/10.5194/bg-19-1225-2022>
- Beguería, S., Vicente-Serrano, S. M., & Beguería, M. S. (2017). Package 'spei', calculation of the Standardised precipitation- evapotranspiration index. Retrieved from <https://cran.r-project.org/web/packages/SPEI/SPEI.pdf>

Acknowledgments

This work was funded by the Netherlands Polar Programme of the Dutch Research Council (NWO) under grant ALWPP.2016.008. The authors thank Leopold Romeijn of Satellite Imaging Corporation for consultation on atmospheric compensation of WorldView and GeoEye images.

- Berner, L. T., Massey, R., Jantz, P., Forbes, B. C., Macias-Fauria, M., Myers-Smith, I., et al. (2020). Summer warming explains widespread but not uniform greening in the Arctic tundra biome. *Nature Communications*, *11*(1), 4621. <https://doi.org/10.1038/s41467-020-18479-5>
- Bhatt, U. S., Walker, D. A., Reynolds, M. K., Bieniek, P. A., Epstein, H. E., Comiso, J. C., et al. (2013). Recent declines in warming and vegetation greening trends over pan-Arctic tundra. *Remote Sensing*, *5*(9), 4229–4254. <https://doi.org/10.3390/rs5094229>
- Bhatt, U. S., Walker, D. A., Reynolds, M. K., Comiso, J. C., Epstein, H. E., Jia, G. J., et al. (2010). Circumpolar arctic tundra vegetation change is linked to sea ice decline. *Earth Interactions*, *14*, 1–20. <https://doi.org/10.1175/2010EI1315.1171>
- Biskaborn, B. K., Smith, S. L., Noetzel, J., Matthes, H., Vieira, G., Streletskiy, D. A., et al. (2019). Permafrost is warming at a global scale. *Nature Communications*, *10*, 1–11. <https://doi.org/10.1038/s41467-018-08240-4>
- Blok, D., Sass-Klaassen, U., Schaepman-Strub, G., Heijmans, M., Sauren, P., & Berendse, F. (2011). What are the main climate drivers for shrub growth in Northeastern Siberian tundra? *Biogeosciences*, *8*(5), 1169–1179. <https://doi.org/10.5194/bg-8-1169-2011>
- Blok, D., Schaepman-Strub, G., Bartholomeus, H., Heijmans, M., Maximov, T. C., & Berendse, F. (2011). The response of arctic vegetation to the summer climate: Relation between shrub cover, NDVI, surface albedo and temperature. *Environmental Research Letters*, *6*(3), 035502. <https://doi.org/10.1088/1748-9326/6/3/035502>
- Boelman, N. T., Gough, L., McLaren, J. R., & Greaves, H. (2011). Does NDVI reflect variation in the structural attributes associated with increasing shrub dominance in arctic tundra? *Environmental Research Letters*, *6*(3), 035501. <https://doi.org/10.1088/1748-9326/6/3/035501>
- Box, J. E., Colgan, W. T., Christensen, T. R., Schmidt, N. M., Lund, M., Parmentier, F. J. W., et al. (2019). Key indicators of arctic climate change: 1971–2017. *Environmental Research Letters*, *14*(4), 045010. <https://doi.org/10.1088/1748-9326/aaf1b>
- Chen, Y., Liu, A., & Cheng, X. (2021). Vegetation grows more luxuriantly in Arctic permafrost drained lake basins. *Global Change Biology*, *27*(22), 5865–5876. <https://doi.org/10.1111/gcb.15853>
- Clifford, P., Richardson, S., & Hemon, D. (1989). Assessing the significance of the correlation between two spatial processes. *Biometrics*, *45*, 123–134. <https://doi.org/10.2307/2532039>
- Collow, A. B. M., Thomas, N. P., Bosilovich, M. G., Lim, Y.-K., Schubert, S. D., & Koster, R. D. (2022). Seasonal variability in the mechanisms behind the 2020 Siberian heatwaves. *Journal of Climate*, *35*(10), 1–3090. <https://doi.org/10.1175/JCLI-D-21-0432.1>
- Douglas, T. A., Turetsky, M. R., & Koven, C. D. (2020). Increased rainfall stimulates permafrost thaw across a variety of Interior Alaskan boreal ecosystems. *NPJ Climate and Atmospheric Science*, *3*, 1–7. <https://doi.org/10.1038/s41612-020-0130-4>
- Dutilleul, P., Clifford, P., Richardson, S., & Hemon, D. (1993). Modifying the *t* test for assessing the correlation between two spatial processes. *Biometrics*, *49*, 305–314. <https://doi.org/10.2307/2532625>
- Evans, J. S., & Ram, K. (2021). Package 'spatialEco'. R CRAN Project. Retrieved from <https://cran.r-project.org/web/packages/spatialEco/spatialEco.pdf>
- Fedorov, A. N., Vasilyev, N. F., Torgovkin, Y. I., Shestakova, A. A., Varlamov, S. P., Zheleznyak, M. N., et al. (2018). Permafrost-landscape map of the Republic of Sakha (Yakutia) on a scale 1: 1,500,000. *Geosciences*, *8*(12), 465. <https://doi.org/10.3390/geosciences8120465>
- Fernandes, R., & Leblanc, S. G. (2005). Parametric (modified least squares) and non-parametric (Theil–Sen) linear regressions for predicting biophysical parameters in the presence of measurement errors. *Remote Sensing of Environment*, *95*(3), 303–316. <https://doi.org/10.1016/j.rse.2005.01.005>
- Forbes, B. C., Fauria, M. M., & Zetterberg, P. (2010). Russian Arctic warming and 'greening' are closely tracked by tundra shrub willows. *Global Change Biology*, *16*(5), 1542–1554. <https://doi.org/10.1111/j.1365-2486.2009.02047.x>
- Forkel, M., Carvalhais, N., Verbesselt, J., Mahecha, M. D., Neigh, C. S., & Reichstein, M. (2013). Trend change detection in NDVI time series: Effects of inter-annual variability and methodology. *Remote Sensing*, *5*, 2113–2144. <https://doi.org/10.3390/rs5052113>
- Fortin, M.-J., & Payette, S. (2002). How to test the significance of the relation between spatially autocorrelated data at the landscape scale: A case study using fire and forest maps. *Écoscience*, *9*(2), 213–218. <https://doi.org/10.1080/11956860.2002.11682707>
- Frost, G., Bhatt, U., Macander, M., Hendricks, A., & Jorgenson, M. (2021). Is Alaska's Yukon–Kuskokwim delta greening or browning? Resolving mixed signals of tundra vegetation dynamics and drivers in the maritime arctic. *Earth Interactions*, *25*(1), 76–93. <https://doi.org/10.1175/EI-D-20-0025.1>
- Frost, G., Macander, M., Bhatt, U., Berner, L., Bjerke, J., Epstein, H., et al. (2021). Tundra greenness. *Arctic Report Card 2021*. <https://doi.org/10.25923/8n78-wp73>
- Fujinami, H., Yasunari, T., & Watanabe, T. (2016). Trend and interannual variation in summer precipitation in eastern Siberia in recent decades. *International Journal of Climatology*, *36*(1), 355–368. <https://doi.org/10.1002/joc.4352>
- Gorelick, N., Hancher, M., Dixon, M., Ilyushchenko, S., Thau, D., & Moore, R. (2017). Google Earth engine: Planetary-scale geospatial analysis for everyone. *Remote Sensing of Environment*, *202*, 18–27. <https://doi.org/10.1016/j.rse.2017.06.031>
- Goswami, S., Gamon, J. A., & Tweedie, C. E. (2011). Surface hydrology of an arctic ecosystem: Multiscale analysis of a flooding and draining experiment using spectral reflectance. *Journal of Geophysical Research*, *116*, G00I07. <https://doi.org/10.1029/2010jg001346>
- Grosse, G., Romanovsky, V., Walter, K., Morgenstern, A., Lantuit, H., & Zimov, S. (2008). Distribution of thermokarst lakes and ponds at three Yedoma sites in Siberia. In D. L. Kane & K. M. Hinkel (Eds.), *Ninth international conference on permafrost*. Institute of Northern Engineering, University of Alaska Fairbanks. <https://doi.org/10.1013/epic.31102.d001>
- Haverkamp, P. J., Bysykatova-Harmey, I., Germogenov, N., & Schaepman-Strub, G. (2022). Increasing Arctic Tundra flooding threatens wildlife habitat and survival: Impacts on the critically endangered Siberian Crane (*Grus leucogeranus*). *Frontiers in Conservation Science*, *3*, 799998. <https://doi.org/10.3389/fcosc.2022.799998>
- Heijmans, M. M. P. D., Magnússon, R. Í., Lara, M. J., Frost, G. V., Myers-Smith, I. H., Van Huissteden, J., et al. (2022). Tundra vegetation change and impacts on permafrost. *Nature Reviews Earth & Environment*, *3*(1), 68–84. <https://doi.org/10.1038/s43017-021-00233-0>
- Hesselbarth, M. H., Sciacini, M., With, K. A., Wiegand, K., & Nowosad, J. (2019). Landscapemetrics: An open-source R tool to calculate landscape metrics. *Ecography*, *42*(10), 1648–1657. <https://doi.org/10.1111/ecog.04617>
- HSAF. (2020). Scatterometer root zone soil moisture (RZSM) data record 10 km resolution – multimission. EUMETSAT SAF on Support to Operational Hydrology and Water Management [dataset]. https://doi.org/10.15770/EUM_SAF_H_0008
- IPCC. (2021). In V. Masson-Delmotte, P. Zhai, A. Pirani, S. L. Connors, C. Péan, S. Berger, et al. (Eds.), *Climate change 2021: The physical science basis. contribution of working group I to the sixth assessment report of the intergovernmental panel on climate change*. Masson-delmotte. Cambridge University Press. <https://doi.org/10.1017/9781009157896.2391>
- Iwahana, G., Takano, S., Petrov, R. E., Tei, S., Shingubara, R., Maximov, T. C., et al. (2014). Geocryological characteristics of the upper permafrost in a tundra-forest transition of the Indigirka River Valley, Russia. *Polar Science*, *8*(2), 96–113. <https://doi.org/10.1016/j.polar.2014.01.005>
- Jones, B. M., Grosse, G., Farquharson, L. M., Roy-Léveillé, P., Veremeeva, A., Kanevskiy, M. Z., et al. (2022). Lake and drained lake basin systems in lowland permafrost regions. *Nature Reviews Earth & Environment*, *3*(1), 85–98. <https://doi.org/10.1038/s43017-021-00238-9>
- Jorgenson, M. T., & Shur, Y. (2007). Evolution of lakes and basins in northern Alaska and discussion of the thaw lake cycle. *Journal of Geophysical Research*, *112*(F2), F02S17. <https://doi.org/10.1029/2006JF000531>

- Karami, M., Westergaard-Nielsen, A., Normand, S., Treier, U. A., Elberling, B., & Hansen, B. U. (2018). A phenology-based approach to the classification of Arctic tundra ecosystems in Greenland. *ISPRS Journal of Photogrammetry and Remote Sensing*, *146*, 518–529. <https://doi.org/10.1016/j.isprsjprs.2018.11.005>
- Komsta, L., & Komsta, M. L. (2013). Package 'mblm'. Retrieved from <https://cran.r-project.org/web/packages/mblm/mblm.pdf>
- Lara, M. J., Nitze, I., Grosse, G., Martin, P., & McGuire, A. D. (2018). Reduced arctic tundra productivity linked with landform and climate change interactions. *Scientific Reports*, *8*(1), 2345. <https://doi.org/10.1038/s41598-018-20692-8>
- Li, B., Heijmans, M. M. P. D., Blok, D., Wang, P., Karsanaev, S. V., Maximov, T. C., et al. (2017). Thaw pond development and initial vegetation succession in experimental plots at a Siberian lowland tundra site. *Plant and Soil*, *420*(1–2), 147–162. <https://doi.org/10.1007/s11104-017-3369-8>
- Li, J., Holmgren, M., & Xu, C. (2021). Greening vs browning? Surface water cover mediates how tundra and boreal ecosystems respond to climate warming. *Environmental Research Letters*, *16*(10), 104004. <https://doi.org/10.1088/1748-9326/ac2376>
- Lin, D., Johnson, D., Andresen, C., & Tweedie, C. (2012). High spatial resolution decade-time scale land cover change at multiple locations in the Beringian Arctic (1948–2000s). *Environmental Research Letters*, *7*(2), 025502. <https://doi.org/10.1088/1748-9326/7/2/025502>
- Lorant, M. M., Goetz, S. J., & Beck, P. S. (2011). Tundra vegetation effects on pan-Arctic albedo. *Environmental Research Letters*, *6*(2), 024014. <https://doi.org/10.1088/1748-9326/6/2/024014>
- Magnússon, R. Í., Hamm, A., Karsanaev, S. V., Limpens, J., Kleijn, D., Frampton, A., et al. (2022). Extremely wet summer events enhance permafrost thaw for multiple years in Siberian tundra. *Nature Communications*, *13*, 1–10. <https://doi.org/10.1038/s41467-022-29248-x>
- Magnússon, R. Í., Limpens, J., Kleijn, D., Van Huissteden, K., Maximov, T. C., Lobry, S., & Heijmans, M. M. P. D. (2021). Shrub decline and expansion of wetland vegetation revealed by very high resolution land cover change detection in the Siberian lowland tundra. *Science of The Total Environment*, *782*, 146877. <https://doi.org/10.1016/j.scitotenv.2021.146877>
- Main-Knorn, M., Pflug, B., Louis, J., Debaecker, V., Müller-Wilm, U., & Gascon, F. (2017). Sen2Cor for sentinel-2, image and signal processing for remote sensing XXIII, 1042704. *Image and Signal Processing for Remote Sensing XXIII*, 10427. <https://doi.org/10.1117/12.2278218>
- Martin, A. C., Jeffers, E. S., Petrokofsky, G., Myers-Smith, I., & Macias-Fauria, M. (2017). Shrub growth and expansion in the arctic tundra: An assessment of controlling factors using an evidence-based approach. *Environmental Research Letters*, *12*(8), 085007. <https://doi.org/10.1088/1748-9326/aa7989>
- Maxar. (n.d.). Atmospheric compensation - MAXAR AComp pre-processing. Retrieved from <https://www.satimagingcorp.com/services/atmospheric-compensation>, last access: 29-04-2022.
- McGuire, A. D., Lawrence, D. M., Koven, C., Clein, J. S., Burke, E., Chen, G., et al. (2018). Dependence of the evolution of carbon dynamics in the northern permafrost region on the trajectory of climate change. *Proceedings of the National Academy of Sciences*, *115*(15), 3882–3887. <https://doi.org/10.1073/pnas.1719903115>
- Mekonnen, Z. A., Riley, W. J., Berner, L. T., Bouskill, N. J., Torn, M. S., Iwahana, G., et al. (2021). Arctic tundra shrubification: A review of mechanisms and impacts on ecosystem carbon balance. *Environmental Research Letters*, *16*(5), 053001. <https://doi.org/10.1088/1748-9326/abf28b>
- Meredith, M., Sommerkorn, M., Cassotta, S., Derksen, C., Ekaykin, A., Hollowed, A., et al. (2019). Polar regions. In H.-O. Pörtner, D. C. Roberts, V. Masson-Delmotte, P. Zhai, M. Tignor, E. Poloczanska, et al. (Eds.), *IPCC special report on the ocean and cryosphere in a changing climate* (pp. 203–320). Cambridge University Press. <https://doi.org/10.1017/9781009157964.005>
- Morgenstern, A., Ulrich, M., Günther, F., Roessler, S., Fedorova, I. V., Rudaya, N. A., et al. (2013). Evolution of thermokarst in East Siberian ice-rich permafrost: A case study. *Geomorphology*, *201*, 363–379. <https://doi.org/10.1016/j.geomorph.2013.07.011>
- Myers-Smith, I. H., Kerby, J. T., Phoenix, G. K., Bjerke, J. W., Epstein, H. E., Assmann, J. J., et al. (2020). Complexity revealed in the greening of the Arctic. *Nature Climate Change*, *10*(2), 106–117. <https://doi.org/10.1038/s41558-019-0688-1>
- National Academies of Sciences, Engineering and Medicine. (2019). *Understanding northern latitude vegetation greening and browning: Proceedings of A Workshop* (p. 62). The National Academies Press. <https://doi.org/10.17226/25423>
- Nauta, A. L., Heijmans, M. M., Blok, D., Limpens, J., Elberling, B., Gallagher, A., et al. (2015). Permafrost collapse after shrub removal shifts tundra ecosystem to a methane source. *Nature Climate Change*, *5*(1), 67–70. <https://doi.org/10.1038/NCLIMATE2446>
- Nitzbon, J., Westermann, S., Langer, M., Martin, L. C. P., Strauss, J., Laboor, S., & Boike, J. (2020). Fast response of cold ice-rich permafrost in northeast Siberia to a warming climate. *Nature Communications*, *11*(1), 2201. <https://doi.org/10.1038/s41467-020-15725-8>
- Nitze, I., & Grosse, G. (2016). Detection of landscape dynamics in the Arctic Lena Delta with temporally dense Landsat time-series stacks. *Remote Sensing of Environment*, *181*, 27–41. <https://doi.org/10.1016/j.rse.2016.03.038>
- Osorio, F., Vallejos, R., Cuevas, F., Mancilla, D., & Osorio, M. F. (2020). Package 'SpatialPack'. Retrieved from <https://cran.r-project.org/web/packages/SpatialPack/SpatialPack.pdf>
- Overland, J. E., & Wang, M. (2021). The 2020 Siberian heat wave. *International Journal of Climatology*, *41*(S1), E2341–E2346. <https://doi.org/10.1002/joc.6850>
- Pacifici, F., Longbotham, N., & Emery, W. J. (2014). The importance of physical quantities for the analysis of multitemporal and multian-gular optical very high spatial resolution images. *IEEE Transactions on Geoscience and Remote Sensing*, *52*(10), 6241–6256. <https://doi.org/10.1109/TGRS.2013.2295819>
- Pekel, J.-F., Cottam, A., Gorelick, N., & Belward, A. S. (2016). High-resolution mapping of global surface water and its long-term changes. *Nature*, *540*(7633), 418–422. <https://doi.org/10.1038/nature20584>
- Phoenix, G. K., & Bjerke, J. W. (2016). Arctic browning: Extreme events and trends reversing arctic greening. *Global Change Biology*, *22*(9), 2960–2962. <https://doi.org/10.1111/gcb.13261>
- Porter, C., Morin, P., Howat, I., Noh, M.-J., Bates, B., Peterman, K., et al. (2018). ArcticDEM. *Harvard Dataverse*, *1*, 2018–2030. <https://doi.org/10.7910/DVN/OHHUKH>
- Potts, R. (1952). Some generalized order-disorder transformations. *Mathematical Proceedings of the Cambridge Philosophical Society*, *48*(1), 106–109. <https://doi.org/10.1017/S0305004100027419>
- Raynolds, M. K., & Walker, D. A. (2016). Increased wetness confounds Landsat-derived NDVI trends in the central Alaska North Slope region, 1985–2011. *Environmental Research Letters*, *11*(8), 085004. <https://doi.org/10.1088/1748-9326/11/8/085004>
- Raynolds, M. K., Walker, D. A., Balsler, A., Bay, C., Campbell, M., Cherosov, M. M., et al. (2019). A raster version of the circumpolar arctic vegetation map (CAVM). *Remote Sensing of Environment*, *232*, 111297. <https://doi.org/10.1016/j.rse.2019.111297>
- Rihmi-Wdc (2020). All-Russian research institute of hydrometeorological information - World Data Centre. Retrieved from <http://aisori-m.meteo.ru/waisori>
- Roach, J., Griffith, B., Verbyla, D., & Jones, J. (2011). Mechanisms influencing changes in lake area in Alaskan boreal forest. *Global Change Biology*, *17*(8), 2567–2583. <https://doi.org/10.1111/j.1365-2486.2011.02446.x>

- Roy, D. P., Kovalskyy, V., Zhang, H., Vermote, E. F., Yan, L., Kumar, S., & Egorov, A. (2016). Characterization of landsat-7 to landsat-8 reflective wavelength and normalized difference vegetation index continuity. *Remote sensing of Environment*, *185*, 57–70. <https://doi.org/10.1016/j.rse.2015.12.024>
- Schubert, P., Eklundh, L., Lund, M., & Nilsson, M. (2010). Estimating northern peatland CO₂ exchange from MODIS time series data. *Remote Sensing of Environment*, *114*(6), 1178–1189. <https://doi.org/10.1016/j.rse.2010.01.005>
- Sen, P. K. (1968). Estimates of the regression coefficient based on Kendall's tau. *Journal of the American Statistical Association*, *63*(324), 1379–1389. <https://doi.org/10.1080/01621459.1968.10480934>
- Shkolnik, I., Pavlova, T., Efimov, S., & Zhuravlev, S. (2018). Future changes in peak river flows across northern Eurasia as inferred from an ensemble of regional climate projections under the IPCC RCP8.5 scenario. *Climate Dynamics*, *50*(1–2), 215–230. <https://doi.org/10.1007/s00382-017-3600-6>
- Siewert, M. B., Hanisch, J., Weiss, N., Kuhry, P., Maximov, T. C., & Hugelius, G. (2015). Comparing carbon storage of Siberian tundra and taiga permafrost ecosystems at very high spatial resolution. *Journal of Geophysical Research: Biogeosciences*, *120*(10), 1973–1994. <https://doi.org/10.1002/2015JG002999>
- Storey, J., Lacasse, J., Smilek, R., Zeiler, T., Scaramuzza, P., Rengarajan, R., & Choate, M. (2005). Image impact of the landsat 7 ETM+ scan line corrector failure.
- Tei, S., Morozumi, T., Nagai, S., Takano, S., Sugimoto, A., Shingubara, R., et al. (2020). An extreme flood caused by a heavy snowfall over the Indigirka River basin in Northeastern Siberia. *Hydrological Processes*, *34*(3), 522–537. <https://doi.org/10.1002/hyp.13601>
- Theil, H. (1950). A rank-invariant method of linear and polynomial regression analysis. *Proceeding of National Academy of Sciences USA*, *53*. Part I: 386–392, Part II: 521–525, Part III: 1397–1412.
- Treharne, R., Bjerke, J. W., Tømmervik, H., Stendardi, L., & Phoenix, G. K. (2019). Arctic browning: Impacts of extreme climatic events on heathland ecosystem CO₂ fluxes. *Global Change Biology*, *25*(2), 489–503. <https://doi.org/10.1111/gcb.14500>
- Troeva, E. I., Isaev, A. P., Cherosov, M. M., & Karpov, N. (2010). *The far north: Plant biodiversity and ecology of Yakutia* (p. 401). Springer Science & Business Media. <https://doi.org/10.1007/978-90-481-3774-9>
- Tucker, C. J. (1979). Red and photographic infrared linear combinations for monitoring vegetation. *Remote sensing of Environment*, *8*(2), 127–150. [https://doi.org/10.1016/0034-4257\(79\)90013-0](https://doi.org/10.1016/0034-4257(79)90013-0)
- Turetsky, M. R., Abbott, B. W., Jones, M. C., Walter Anthony, K., Olefeldt, D., Schuur, E. A. G., et al. (2020). Carbon release through abrupt permafrost thaw. *Nature Geoscience*, *13*(2), 138–143. <https://doi.org/10.1038/s41561-019-0526-0>
- Van der Molen, M., Van Huissteden, J., Parmentier, F., Petrescu, A., Dolman, A., Maximov, T., et al. (2007). The growing season greenhouse gas balance of a continental tundra site in the Indigirka lowlands, NE Siberia. *Biogeosciences*, *4*(6), 985–1003. <https://doi.org/10.5194/bg-4-985-2007>
- Van Huissteden, J., & Beletti Marchesini, L. (2014). Geomorphological and cryological map of Kytalyk, Russia, links to shapefiles. Dataset. <https://doi.org/10.1594/PANGAEA.833042>
- Van Huissteden, J., Teshebaeva, K., Cheung, Y., Magnússon, R. Í., Noorbergen, H., Karsanaev, S. V., et al. (2021). Geomorphology and InSAR-tracked surface displacements in an ice-rich Yedoma landscape. *Frontiers in Earth Science*, *9*, 680565. <https://doi.org/10.3389/feart.2021.680565>
- Verdonen, M., Berner, L. T., Forbes, B. C., & Kumpula, T. (2020). Periglacial vegetation dynamics in Arctic Russia: Decadal analysis of tundra regeneration on landslides with time series satellite imagery. *Environmental Research Letters*, *15*(10), 105020. <https://doi.org/10.1088/1748-9326/abb500>
- Vicente-Serrano, S. M., Beguería, S., & López-Moreno, J. I. (2010). A multiscale drought index sensitive to global warming. The standardized precipitation evapotranspiration index. *Journal of Climate*, *23*(7), 1696–1718. <https://doi.org/10.1175/2009jcli2909.1>
- Wang, P., De Jager, J., Nauta, A., Van Huissteden, J., Trofim, M. C., & Limpens, J. (2019). Exploring near-surface ground ice distribution in patterned-ground tundra: Correlations with topography, soil and vegetation. *Plant and Soil*, *444*(1–2), 251–265. <https://doi.org/10.1007/s11104-019-04276-7>
- Wang, P., Huang, Q., Tang, Q., Chen, X., Yu, J., Pozdniakov, S. P., & Wang, T. (2021). Increasing annual and extreme precipitation in permafrost-dominated Siberia during 1959–2018. *Journal of Hydrology*, *603*, 126865. <https://doi.org/10.1016/j.jhydrol.2021.126865>
- Zona, D., Lafleur, P. M., Hufkens, K., Gioli, B., Bailey, B., Burba, G., et al. (2022). Pan-Arctic soil moisture control on tundra carbon sequestration and plant productivity. *Global Change Biology*, *00*(5), 1–15. <https://doi.org/10.1111/gcb.16487>
- Zona, D., Oechel, W., Peterson, K., Clements, R., Paw U, K. T., & Ustin, S. (2010). Characterization of the carbon fluxes of a vegetated drained lake basin chronosequence on the Alaskan Arctic Coastal Plain. *Global Change Biology*, *16*(6), 1870–1882. <https://doi.org/10.1111/j.1365-2486.2009.02107.x>